H I 21 cm Cosmology and the Bi-spectrum: Closure Diagnostics in Massively Redundant Interferometric Arrays

C.L. Carilli[1,2], Bojan Nikolic[2], Nithyanandan Thyagarajan[1,3]*, K. Gale-Sides[2], Zara Abdurashidova[5], James E. Aguirre[4], Paul Alexander[2], Zaki S. Ali[5], Yanga Balfour[13], Adam P. Beardsley[3], Gianni Bernardi[11,12], Judd D. Bowman[3], Richard F. Bradley[10], Jacob Burba[6], Carina Cheng[5], David R. DeBoer[5], Matt Dexter[5], Eloy de Lera Acedo[2], Joshua S. Dillon[5], Aaron Ewall-Wice[9], Gcobisa Fadana[13], Nicolas Fagnoni[2], Randall Fritz[13], Steve R. Furlanetto[7], Abhik Ghosh[13], Brian Glendenning[1], Bradley Greig[12], Jasper Grobbelaar[13], Ziyaad Halday[13], Bryna J. Hazelton[14,15], Jacqueline N. Hewitt[9], Jack Hickish[5], Daniel C. Jacobs[3], Austin Julius[13], MacCalvin Kariseb[13], Saul A. Kohn[4], Mathew Kolopanis[3], Telalo Lekalake[13], Adrian Liu[5,†], Anita Loots[13], David MacMahon[5], Lourence Malan[13], Cresshim Malgas[13], Matthys Maree[13], Zachary Martinot[4], Eunice Matsetela[13], Andrei Mesinger[12], Mathakane Molewa[13], Miguel F. Morales[14], Abraham R. Neben[9], Aaron R. Parsons[5], Nipanjana Patra[5], Samantha Pieterse[13], Paul La Plante[4], Jonathan C. Pober[6], Nima Razavi-Ghods[2], Jon Ringuette[14], James Robnett[1], Kathryn Rosie[13], Raddwine Sell[13], Peter Sims[6], Craig Smith[13], Angelo Syce[13], Peter K. G. Williams[8], Haoxuan Zheng[9]

[1]National Radio Astronomy Observatory, P. O. Box 0, Socorro, NM 87801, USA
[2]Astrophysics Group, Cavendish Laboratory, JJ Thomson Avenue, Cambridge CB3 0HE, UK
[3]Arizona State University, School of Earth and Space Exploration, Tempe, AZ 85287, USA
[4]Department of Physics and Astronomy, University of Pennsylvania, Philadelphia, PA
[5]Department of Astronomy, University of California, Berkeley, CA, USA
[6]Physics Department, Brown University, Providence, RI
[7]Department of Physics and Astronomy, University of California, Los Angeles, CA
[8]Harvard-Smithsonian Center for Astrophysics, Cambridge, MA
[9]Department of Physics, Massachusetts Institute of Technology, Cambridge, MA
[10]National Radio Astronomy Observatory, Charlottesville, VA
[11]Department of Physics and Electronics, Rhodes University, Grahamstown, South Africa
[12]Scuola Normale Superiore, Pisa, Italy
[13]SKA-SA, Cape Town, South Africa
[14]Department of Physics, University of Washington, Seattle, WA
[15]eScience Institute, University of Washington, Seattle, WA

Key Points:

- New massively redundant low frequency arrays allow for a novel investigation of closure relations in radio interferometry.
- We use closure phase spectra for redundant triads to estimate departures from redundancy for redundant baseline visibilities.
- We investigate the temporal behaviour of closure spectra, and show that time averaging should be limited to about 1min to 2min, due to transit of the sky through the primary beam of the telescope.
- We show that closure phase spectra can also be used to identify bad antennas in the array, independent of calibration.
- We develop the tools and framework in which closure phase spectra may be used in the search for the H I 21 cm signal from cosmic reionization.

*Nithyanandan Thyagarajan is a Jansky Fellow of the National Radio Astronomy Observatory.

†A. Liu is a Hubble Fellow at UCB

Corresponding author: Chris Carilli, `ccarilli@nrao.edu`

Abstract

New massively redundant low frequency arrays allow for a novel investigation of closure relations in interferometry. We employ commissioning data from the Hydrogen Epoch of Reionization Array to investigate closure quantities in this densely packed grid array of 14m antennas operating at 100 MHz to 200 MHz. We investigate techniques that utilize closure phase spectra for redundant triads to estimate departures from redundancy for redundant baseline visibilities. We find a median absolute deviation from redundancy in closure phase across the observed frequency range of about 4.5°. This value translates into a non-redundancy per visibility phase of about 2.6°, using proto-type electronics. The median absolute deviations from redundancy decrease with longer baselines. We show that closure phase spectra can be used to identify ill-behaved antennas in the array, independent of calibration. We investigate the temporal behaviour of closure spectra. The Allan variance increases after a one minute stride time, due to passage of the sky through the primary beam of the transit telescope. However, the closure spectra repeat to well within the noise per measurement at corresponding local sidereal times (LST) from day to day. In future papers in this series we will develop the technique of using closure phase spectra in the search for the H I 21 cm signal from cosmic reionization.

1 Introduction

Closure quantities have long been a tool in interferometric imaging [*Jennison*, 1958; *Rogers et al.*, 1974]. As is well known, calculation of closure quantities from interferometric visibilities is independent of phase and amplitude terms introduced by antenna optics and electronics (e.g., standing waves), as well as to electrical path length and attenuation contributions due to the ionosphere and troposphere above the antenna. Hence, closure quantities represent a robust measurement of the sky signal, independent of antenna-based calibration and calibration errors [*Johnson et al.*, 2017; *Roelofs et al.*, 2017].

This is the first in a series of papers considering closure measurements, and their application to H I 21 cm cosmology. Low frequency radio astronomy is undergoing a renaissance due to the intensive search for the 21 cm line signal from neutral Hydrogen during the epoch of cosmic reionization, and into the preceding dark ages [*Fan et al.*, 2006; *Morales and Wyithe*, 2010]. These low frequency measurements are complicated by the strong continuum sky signal, coupled to any chromatic response of the telescope. Examination of closure spectra may provide a robust method to detect the H I signal, independent of antenna-based calibration and the ionosphere [*Carilli and Sims*, 2016; *Thyagarajan, Carilli, and Nikolic*, 2018]. Study of the closure spectra also provides powerful, calibration-independent, diagnostics of the array performance [*Carilli and Nikolic*, 2017].

We develop the formalism and tools for making the closure measurements in the context of the massively redundant interferometric transit array, the Hydrogen Epoch of Reionization Array [HERA; *DeBoer et al.*, 2017; *Ewall-Wice et al.*, 2016; *Neben et al.*, 2016; *Patra et al.*, 2017; *Thyagarajan et al.*, 2016]. HERA provides us a unique laboratory to explore closure as an array diagnostic, including measuring the level of redundancy for the baselines, searching for ill-behaved antennas, and measuring the effect on coherent averaging of time variation as the sky transits the array. In the second paper, we will present the cosmological formalism for searching for the H I 21 cm signal using closure measurements [*Thyagarajan, Carilli, and Nikolic*, 2018]. In a third paper, we will apply the technique to HERA observations taken over the 2017-2018 winter. We emphasize at the start that there are non-closing effects, possibly due to polarization leakage, cross coupling of antennas, and non-identical far sidelobes of the telescope beams that can lead to departures from the closure relationship. We consider these in more detail below.

2 H I 21 cm cosmology: context and challenges

Detecting the H I 21 cm line signal from the neutral intergalactic medium during cosmic reionization is one of the paramount goals of modern astrophysics [*Sunyaev and Zeldovich*, 1972; *Scott and Rees*, 1990; *Madau et al.*, 1997; *Tozzi et al.*, 2000; *Iliev et al.*, 2002; *Fan et al.*, 2006; *Barkana and Loeb*, 2007; *Morales and Wyithe*, 2010]. These epochs correspond to the early formation of galaxies, within a few hundred million years of the Big Bang. Current indirect measurements suggest cosmic reionization occurred at $z \sim 6$–10 [*Bañados et al.*, 2017; *Robertson et al.*, 2015; *Greig and Mesinger*, 2017]. Hence, the expected H I 21 cm signal from the epoch of reionization (EoR) will be observed at frequencies from 100 MHz to 200 MHz. Most recently, there is a possible detection of the all-sky HI 21cm signal from the IGM at $z \sim 18$, during the so-called 'cosmic dawn', when the very first generation of stars form [*Bowman et al.*, 2018; *Barkana*, 2018].

Numerous low frequency interferometers and total power experiments have been built with the thermal sensitivity adequate to detect the H I 21 cm signal from the reionization epoch [*Thyagarajan et al.*, 2013; *Beardsley et al.*, 2013; *Monsalve et al.*, 2017]. However, the task is complicated by the much stronger foreground continuum emission: the required dynamic range is about 50dB in the mean brightness [*Monsalve et al.*, 2017], and 40dB for spatial fluctuations on the scales relevant to current interferometric observations [*Sims et al.*, 2016].

A crucial distinguishing property of the foregrounds is that they are dominated by synchrotron radiation. Synchrotron radiation is a non-thermal process, which is well determined in the laboratory and in space to display power-law spectra over a very broad frequency range. Such power-law spectra are featureless over scales of hundreds of MHz [*Pacholczyk*, 1970]. This spectral smoothness is in stark contrast to the H I 21 cm line emission, which fluctuates rapidly in frequency down to kHz scales [*Carilli et al.*, 2002]. A naive solution to remove the continuum foregrounds would be fitting a smoothly varying function (such as a polynomial) in frequency to either the visibilities or the spectral image cubes. However, *Sims et al.* [2016] show that, without *a priori* knowledge of the covariance between the foregrounds and the 21 cm signal in the data, blind subtraction of a foreground model from the data prior to estimation of the quantity of interest will produce biased estimates of said quantity. As such, joint estimation of the foregrounds and 21 cm signal is essential for obtaining statistically robust estimates of the 21 cm signal.

Perhaps more importantly, *Datta et al.* [2009, 2010] show that the chromatic response of an interferometer for very wide-field imaging imprints a spectral signature on the visibility data which is impossible to remove using continuum subtraction techniques via smooth curve-fitting to either the visibility spectra, or position-by-position smooth curve-fitting to a spectral image cube [*Rupen*, 1999].

The continuum can still be removed properly, in theory, through a frequency-dependent subtraction from the visibilities of an accurate continuum model. The challenge, as *Datta et al.* [2010] show, is that such a subtraction requires remarkably accurate complex gain calibration ($\sim 0.1\%$), as a function of frequency [*Datta et al.*, 2009, 2010]. These techniques, as exemplified for example by LOFAR analysis of the reionization signal, are known as 'foreground removal techniques' [*Patil et al.*, 2017]. Progress has been made on foreground removal techniques, using the spectral and spatial characteristics, in particular by [*Trott et al.*, 2016; *Mertens et al.*, 2017], however, a detection of the statistical fluctuations of the HI 21cm signal has not yet been made.

These facts have led to consideration of alternate methods for detecting the H I 21 cm signal, such as 'foreground avoidance' in delay spectra [*Morales et al.*, 2012; *Parsons et al.*, 2012]. The delay spectrum method involves separating H I line from continuum emission in the three-dimensional power spectral space defined by the line of sight (frequency, or equivalently, redshift) distances and the sky-plane (angular) distances. In this space, the maxi-

mum wavenumber (or spectral frequency) for smooth-spectrum continuum emission due to the chromatic response of a given interferometric baseline is set by the maximum delay of the baseline corresponding to sources at the horizon. Hence, the HI 21cm line signal in the line-of-sight direction appears at all wavenumbers, including large wavenumbers (small scales), whereas the continuum emission is limited to a 'wedge' of low wavenumbers determined by the horizon limit, as demonstrated by *Datta et al.* [2010] and analyzed by *Morales et al.* [2012]; *Parsons et al.* [2012]; *Trott et al.* [2012]; *Vedantham et al.* [2012]; *Pober et al.* [2013]; *Thyagarajan et al.* [2013]; *Liu et al.* [2014].

The avoidance method still requires tight control of the spectral response of other parts of the array, such as the antennas and data transmission system, and/or very accurate calibration of the spectral response (bandpass) with time, wide-field effects, spectral structures in the antenna's angular power pattern, and reflections, to avoid coupling the continuum signal to the line, and thereby causing leakage of the continuum signal into the EoR window [e.g., *Thyagarajan et al.*, 2015a,b, 2016; *Pober et al.*, 2016].

In our broader study, we consider an approach for discovering the H I 21 cm signal using the closure phases of the interferometer. A closure phase is a quantity derived from a simple product of the three visibility pairs from three antennas, more generally known as the 'bispectrum'[1] [*Jennison*, 1958; *Kulkarni*, 1989; *Monnier*, 2007]. It was recognized early in the field of both optical and radio interferometry that closure quantities are independent of antenna-based contributions to the measured phases and amplitudes, such as standing waves arising in antenna structures or cables. This independence also applies to the contribution to electrical path length by atmospheric fluctuations above each antenna (principally due to the troposphere in the case of optical or high frequency radio observations, and the ionosphere at low radio frequencies), although such fluctuations are small on the very short baselines of HERA.

Hence, to the degree that the array response is separable into antenna-based terms, closure phases are independent of calibration and calibration errors, as well as independent of the ionosphere, i.e., closure quantities are a robust 'observable' of the true sky signal. This fact was used in early radio interferometry. In particular, closure analysis was an enabling technique in early Very Long Baseline Interferometry (VLBI) experiments, where maintaining phase coherence was problematic [*Pearson and Readhead*, 1984; *Readhead and Wilkinson*, 1978; *Rogers et al.*, 1974], and remains crucial in current submm VLBI analyses [*Johnson et al.*, 2017; *Roelofs et al.*, 2017]. Closure quantities are still used extensively in optical interferometric image reconstruction [*Thiebaut and Giovannelli*, 2010], as well as being a primary diagnostic for antenna-based calibration errors in phase-connected radio interferometers [*Perley*, 1999].

3 Closure Phase Review

We briefly review the definition of closure phase [see *Cornwell and Fomalont*, 1999; *Thompson et al.*, 2017, for more detail].

3.1 Mathematical foundation

A radio-interferometer measures the time-averaged cross correlation of the electric field voltages from pairs of antennas. Setting aside the polarization of the electric field for the moment, the quasi-monochromatic response of the interferometer can be derived from

---

[1] The bispectrum is a well known statistical tool to study e.g., cosmological anisotropies [*Song et al.*, 2015]. However, such cosmological analyses only consider the scalar amplitudes of the bispectrum, not the vector phases [*Hashimoto et al.*, 2017].

the van Cittert-Zernike theorem as given by *Thompson et al.* [2017]:

$$\mathcal{V}_{ab} = \int d\Omega F_a(\sigma)F_b^*(\sigma)I(\sigma)e^{-j2\pi\mathbf{d}_{ab}\cdot\mathbf{s}} \tag{1}$$

where $\mathcal{V}_{ab}$ is the response ('visibility') measured between antennas number a and b, $d\Omega$ is an infinitesimal element of solid angle, $F_a(\mathbf{s})$ is the antenna voltage response pattern of antenna a in direction of the unit vector $\mathbf{s}$, $I(\mathbf{s})$ is the intensity of radiation from direction $\mathbf{s}$, and $\mathbf{d}_{ab}$ is the vector of between positions of antenna a and b measured in wavelengths of the radiation being received. In practice, any measurement will be an integral over a finite frequency band and sum over polarization states of the incident field.

The 'bi-spectrum' or 'triple product' for an interferometric measurement for antennas a, b and c is defined as:

$$\mathcal{C}_{abc} = \mathcal{V}_{ab}\mathcal{V}_{bc}\mathcal{V}_{ca}. \tag{2}$$

There are two regimes in which this quantity has particularly simple properties and from which stems its practical use.

The first regime of interest is when there is a single point source in direction $\mathbf{s}$ which dominates the received incoming radiation; in this case the integral Eq (1) reduces to:

$$\mathcal{V}_{ab} = F_a(\mathbf{s})F_b^*(\mathbf{s})I_{\mathbf{s}}e^{-j2\pi\mathbf{d}_{ab}\cdot\mathbf{s}} \tag{3}$$

and the triple product is:

$$\begin{aligned}
\mathcal{C}_{abc} &= |F_a(\mathbf{s})|^2\,|F_b(\mathbf{s})|^2\,|F_c(\mathbf{s})|^2\,e^{-j2\pi(\mathbf{d}_{ab}+\mathbf{d}_{bc}+\mathbf{d}_{ca})\cdot\mathbf{s}} \tag{4}\\
&= |F_a(\mathbf{s})|^2\,|F_b(\mathbf{s})|^2\,|F_c(\mathbf{s})|^2 \tag{5}
\end{aligned}$$

where Eq (5) follows because $\mathbf{d}_{ab}$, $\mathbf{d}_{bc}$ and $\mathbf{d}_{ca}$ form a closed triangle and therefore add to null. The phase of $\mathcal{C}_{abc}$ (which is normally referred to as the 'closure phase') is evidently zero in this case entirely independently of the responses of the individual antennas.

The second regime of interest is when the responses of each antenna differ by only a (complex) constant factor that is independent of direction, i.e., $F_a(\mathbf{s}) = F_a'\,F(\mathbf{s})$. The triple product is then

$$\begin{aligned}
\mathcal{C}_{abc} &= \left|F_a'\right|^2\left|F_b'\right|^2\left|F_c'\right|^2 \int d\Omega\,|F(\mathbf{s})|^2\,I(\mathbf{s})e^{-j2\pi\mathbf{d}_{ab}\cdot\mathbf{s}} \times\\
&\quad \times \int d\Omega\,|F(\mathbf{s})|^2\,I(\mathbf{s})e^{-j2\pi\mathbf{d}_{bc}\cdot\mathbf{s}} \times \int d\Omega\,|F(\mathbf{s})|^2\,I(\mathbf{s})e^{-j2\pi\mathbf{d}_{ca}\cdot\mathbf{s}} \tag{6}
\end{aligned}$$

It is again evident that the closure phase, i.e, the phase of the triple product, is independent of the individual antenna responses F_a', F_b' and F_c'. In this case however the phase will not be zero in general and will depend on the sky brightness distribution and the angular dependence of the antenna response pattern.

We emphasize that there are non-closing effects that impact the assumptions made above. We discuss these in depth in §4.2. There is an analogous quantity, the 'closure amplitude' [*Cornwell and Fomalont*, 1999; *Johnson et al.*, 2017], based on the combination of four visibility measurements for which *amplitude* is independent of the antenna-based variation in antenna response. We discuss this closure amplitude briefly in §5.7.

3.2 Use of closure phase

Closure phase is used both as a diagnostic and in inference of the sky brightness distribution. Its use as a diagnostic depends on the property shown in Eq (5), i.e., when a single point source dominates a perfect interferometer will measure zero closure phase regardless of the individual antenna responses. The antenna response includes the many mechanical,

electrical and most atmospheric effects that affect the response of the antenna to celestial radiation and are either not known or are time variable.

Most general purpose radio telescopes observing at cm or shorter wavelengths are made of steerable high-directivity antennas, and the sky at these wavelengths has pronounced point-like sources, it is usually possible to make an observation that satisfies the condition of a single dominant source. The closure phase then provides a direct diagnostic of the interferometer without need for calibration of the unknown or time variable effects, and indeed without the need for any sophisticated post processing of the measured visibilities.

Use of closure phase in constraining models of the sky depends on the property of Eq (6), i.e., that the phase is independent of any unknown or time-varying properties of the antennas that are independent of the angle of arrival of the radiation. The measured closure phase is then a property of the sky and the known angular dependence of the antenna reception pattern only, and can be used to constrain models of the sky without the need for calibration. This use of closure phase was recognized early in the field of astronomical interferometry [*Jennison*, 1958] and is still often used in situations where instrumental phase stability and determination of antenna-based calibration terms may be difficult, such as in certain historical VLBI applications, and in interferometry at optical wavelengths.

We explore the use of closure phase as a diagnostic when the condition of a single dominant point source *is not* met. In this case we do not know *a-priori* the expected closure phase. We can however expect that redundant triads should measure the *same* closure phase. More precisely $C_{abc} = C_{def}$ if $\mathbf{d}_{ab} = \mathbf{d}_{de}$, $\mathbf{d}_{bc} = \mathbf{d}_{ef}$ and $\mathbf{d}_{ca} = \mathbf{d}_{fd}$. In the new generation of highly-redundant interferometric arrays, there are many such redundant triads.

A real interferometer will introduce both thermal noise and complex gain terms, G_i (amplitude and phase terms due to the instrument response; note that this response includes path length differences due to the ionosphere above each antenna [*Mevius et al.*, 2016], that will alter the sky visibility, resulting in a measured quantity, $\mathcal{V}^{\mathrm{m}}_{i,j}(u, v)$:

$$\mathcal{V}^{\mathrm{m}}_{i,j} \quad = G_i G^*_j \mathcal{V}^{\mathrm{s}}_{i,j} = a_i e^{i\theta_i} a_j e^{-i\theta_j} A^s_{i,j} e^{i\phi^s_{i,j}} \quad + \quad N_{i,j} \tag{7}$$

where $A^s_{i,j}$ is the true sky visibility amplitude, $\phi^s_{i,j}$ is the sky visibility phase, and θ_i is the phase introduced to the visibility by the antenna electronics, optics, or ionosphere, $N_{i,j}$ is the noise added to the visibility, $\mathcal{V}^{\mathrm{s}}_{i,j}$ is the effective sky visibility[2], and a_i is the gain amplitude of the antenna plus electronics. This assumes that the complex gain on a given visibility is separable into antenna-based terms.

From this, we can see that the resulting measured visibility phase is the sum of exponents:

$$\phi^{\mathrm{m}}_{i,j} \quad = \phi^{\mathrm{s}}_{i,j} + (\theta_i - \theta_j) + \phi^{\mathrm{n}}_{i,j} \tag{8}$$

where, $\phi^{\mathrm{n}}_{i,j}$ is the noise in the measured visibility phase.

Again, the 'bi-spectrum' or 'triple product' for an interferometric measurement is defined as:

$$C^{\mathrm{m}}_{i,j,k} \quad = \mathcal{V}^{\mathrm{m}}_{i,j} \mathcal{V}^{\mathrm{m}}_{j,k} \mathcal{V}^{\mathrm{m}}_{k,i} \tag{9}$$

---

[2] The true sky visibility set by the sky intensity distribution multiplied by the primary beam power pattern $\equiv A^s_{i,j} e^{i\phi^s_{i,j}}$

It is easy to see from the equations above that the phase of this complex measurement, or closure phase, is, again, the sum of exponents, ie. the sum of the three measured visibility phases:

$$\phi_{i,j,k}^{\mathrm{m}} \quad = \phi_{i,j}^{\mathrm{s}} + (\theta_i - \theta_j) + \phi_{j,k}^{\mathrm{s}} + (\theta_j - \theta_k) + \phi_{k,i}^{\mathrm{s}} + (\theta_k - \theta_i) + \phi_{i,j,k}^{\mathrm{n}} \tag{10}$$

where, $\phi_{i,j,k}^{\mathrm{n}}$ is the noise in the measured closure phase.

The antenna based phase terms then cancel in such a sum, leading to:

$$\phi_{i,j,k}^{\mathrm{m}} \quad = \phi_{i,j,k}^{\mathrm{s}} + \phi_{i,j,k}^{\mathrm{n}}. \tag{11}$$

The closure phase is schematically illustrated in Figure 1. The implication is that the measured closure phase is *independent of antenna-based calibration terms of the form given in the equations above*, and represents a direct measurement of the true closure phase due to structure on the sky, modulo the system thermal noise.

The power of the closure phase spectral analysis is that it is robust to multiplicative contributions to the sky signal which can be separable into antenna gains, as per the historic standard interferometric sky calibration process [*Perley*, 1999], since these cancel in the closure triad calculation. The closure quantity is a true measure of the sky, independent of antenna-base gains. For comparison, redundant visibility spectra are not robust to such antenna-based contributions, and hence are not a true measure of the sky until after calibration is applied. As an example, if there were a strong, and varying, standing wave in the RF/IF bandpass response in one antenna, this will adversely affect the visibilities, and preclude a sky-based measurement without first accurate calibration of the standing wave, but this standing wave would be unseen in the closure analysis. The closure spectrum remains a true sky measurement. The most recent application of closure measurements as a robust sky measurement independent of antenna-base calibration involves interferometric measurements of the supermassive Black Hole at the Galactic center. These include millimeter and submm VLBI measurements, in which time variations of the phase contributions of the antenna electronics, and/or the troposphere, preclude accurate antenna-based calibration [*Roelofs et al.*, 2017; *Johnson et al.*, 2017].

Of course, this conclusion relies on the assumption that the phase induced by the system is factorizable into antenna-based terms, i.e., that the correlator or other aspects of the system do not introduce phase terms that depend on the particular cross-correlation for a visibility. Such non-closing terms are known as 'closure errors', and remain an important diagnostic of the quality of antenna-based calibration in interferometers [*Fomalont and Perley*, 1999], and the ultimate limitation to high dynamic range imaging using hybrid-mapping [*Pearson and Readhead*, 1984].

4 The HERA Array and Data Processing

4.1 The Array

HERA is a close-packed grid of 14 m-diameter parabolic transit reflectors currently observing in the band 100–200 MHz in the Karoo Radio Quiet Preserve in South Africa [*DeBoer et al.*, 2017] at a latitude of $-30.73°$. The array design is optimized for both the redundant spacing calibration technique, and for the delay spectrum technique for detection of the H I 21 cm signal from cosmic reionization [*Parsons et al.*, 2012; *DeBoer et al.*, 2017]. The primary beam FWHM of the dish is about 8° at 150MHz.

The layout of HERA is a split-core hexagonal grid [*Dillon and Parsons*, 2016], with the smallest spacing between two antennas of 14.6 m. The massively redundant HERA con-

figuration allows for a unique application of closure analysis, both in terms of array diagnostics and tests of redundancy, and potentially in the pursuit of H I 21 cm signal detection using closure spectral analysis. We establish the closure calculation formalism and consider array diagnostics. The cosmological application will be presented in the two subsequent papers in the series.

Figure 2 shows the HERA layout for the data analyzed herein. This array had 47 antennas (henceforth we will refer to this configuration as HERA-47) populating grid locations as determined for the final HERA array. The final array will consist of 350 antennas in the full split-core grid, plus out-riggers to 1 km. Our analysis employs commissioning data using prototype electronics. The system electronics will be upgraded in late 2018, including new broader-band feeds. The techinques developed herein will be employed to characterize the new system, as it is deployed.

4.2 Non-redundancy at low frequencies

A key for HERA is the level of redundancy: how redundant are the redundant baselines in the grid array? Non-redundancy for a grid array could arise from cross-talk among cables, or in the correlator.

Non-redundancy at low frequencies can also arise due to the fact that the sky brightness distribution gets multiplied by the primary beam voltage pattern of each antenna. If these voltage patterns differ between antennas, then the product of voltage patterns will be different for each antenna pair, and hence the 'effective sky' (product of the true sky and the antenna voltage patterns) will differ for each supposedly redundant baseline. If all the antennas were close to identical, then this should be a very minor effect.

In the classic antenna-based calibration process (for example, with the VLA or ALMA), the signal is dominated by the calibrator sources in the center of the field. Hence, any differences in primary beam shape or sidelobe patterns is negligible, and the standard assumptions about antenna-based gain separability are valid.[3]

Antenna-based calibration for low frequency arrays is much more complex since the sky signal essentially fills the whole forward response of the telescopes (main beam and sidelobes); this signal consists of both the diffuse Galactic emission and the extragalactic point sources. Hence, differences in the primary beam voltage patterns over the whole forward response factor directly into differences between measured visibilities for baselines that should be redundant. Such voltage pattern differences could arise due to antenna placement position errors, surface differences between antennas, blockage differences, or antenna feed positions and rotations. Non-redundancy could also arise due to differing wide-field polarization response between antennas [*Smirnov*, 2011; *Bhatnagar and Nityananda*, 2001; *Bhatnagar et al.*, 2003].

Likewise, if the field of view is large, the ionosphere may show structure across the field of view. If these structures are different for different antennas, this could lead to non-closing effects. In the case of HERA-47, the field of view is about 8°, which is larger than the expected sizes for significant structure in the ionosphere of $\sim 1.5^o$ (corresponding to ~ 10km at the height of the troposphere [*Kassim et al.*, 2007]). The short baselines considered here (29 m and shorter), however, mean that all the antennas will see the same ionosphere: the diffracted antenna beams at the height of the atmosphere (where the first Fresnel zone radius is around $\sqrt{\frac{\lambda h}{2\pi}} \sim 200$ m) largely coherently overlap, and the power fluctua-

---

[3] In the old VLA broad band continuum correlator, closure errors arose due to differing bandpass shapes for the analog electronics for each antenna. This bandpass effect is directly analogous to what is being considered for the different primary beam power patterns herein. The new digital IF system for the JVLA has eradicated this problem.

tions of electron density at these short lenghtscales is small [*Gehlot et al.*, 2017]. Hence, the summed effect of the ionosphere should still cancel in a closure calculation.

In cases of baseline-dependent responses for the interferometer, the standard calibration assumption that the complex gains are factorize-able into an amplitude and phase per antenna breaks down. This assumption is inherent to both sky-based and redundant spacing calibration algorithms. In theory, the solution to this problem would be to measure the beams, then iterate through a 'self-calibration to sky model' loop that includes direction dependent gains for all antennas [*Bhatnagar et al.*, 2008; *Smirnov and Tasse*, 2015]. In practice, such a process remains at the limit of computational abilities [*Patil et al.*, 2017].

In summary, discrepancy of visibilities measured on geometrically redundant baselines for an array like HERA can arise due to numerous factors, including boresight or global voltage pattern differences, polarization response differences, and differences in the detailed shape of the voltage pattern away from boresight. At present, we have not determined which type of error is dominant for HERA.

As a final note, if the non-redundancy is caused solely by antenna positions errors, then the closure calculation for each triad itself is still valid, but the assumed redundancy between triads breaks-down. One purpose of this paper is to investigate the closure phases for redundant antenna triads in HERA, thereby getting an estimate of the level of redundancy between supposedly redundant baselines.

4.3 HERA-47 Data and Processing

We investigate closure phase spectra for HERA-47 data from October 2017 [see also *Carilli and Sims*, 2016; *Carilli et al.*, 2016; *Carilli and Nikolic*, 2017]. We analyze standard 10 min data sets in one linear polarization (the 'North' polarization, as defined within the HERA project), for the following fields (Julian day and time).

- 2458043.12552: Observations when the Galactic Center was close to transit. The Galactic Center is at J2000 1745-2900.
- 2458043.24482: A field at RA = 21 hr with two bright sources. The two sources are: PMN J2107-2519 and PMN J2101-2802 with flux densities of 34 Jy and 22 Jy respectively at 150 MHz [*Hurley-Walker et al.*, 2017].
- 2458043.58782: A field at RA = 05 hr with a bright cataloged source in the southern part of the beam. The source is PMN J0522-3628 with a flux density of 74.5 Jy at 150 MHz [*Hurley-Walker et al.*, 2017].

In all cases, the Sun was below the horizon.

The native Miriad format transit data from the correlator were converted to uvfits files using pyuvdata [*Hazelton et al.*, 2017], including fringe-tracking on the zenith at the start of the 10 min data set. The record length for each visibility is 10.7 s. The data were then imported into the Common Astronomy Software Applications (CASA; [*McMullin et al.*, 2007]). Channel-based flagging was employed, based on visibility amplitude spectra.

We then performed self-calibration starting with a point source model for the Galactic Center for delay calibration, and then bandpass calibration using sky models derived from the data itself. This process has been shown to converge to a sky brightness distribution consistent with previous low frequency surveys, as has been documented in *Nikolic et al.* [2017]. We demonstrate below that the closure calculation is independent of calibration, since the calibration process makes strictly antenna-based corrections to the visibilities. Note that direction dependent antenna-based gains may invalidate the closure calculation, as discussed in §4.2. We do not analyze amplitudes herein, so the flux scale was arbitrarily set to unity for the Galactic Center. We do perform a rough flux scale bootstrap using the known sources below.

We have written a new task in CASA called CCLOSURE[4]. This program generates *Python Numpy NPZ* format files with closure phases as a function of frequency for specified triads of antennas. We note that antenna ordering in the closure calculation is critical, i.e., for a given triad, going in opposite direction around the triad leads to a sign change. That is, $\phi_{123} = -\phi_{321}$. The CASA convention for a visibility phase is to always have the lower numbered antenna first. We have checked this sign convention, and the CCLOSURE task performs the proper re-ordering in the calculation, as set by the input parameters. The output *npz* files contain information on the channel flags, the closure phases per channel per integration period, and the triads employed. We have written python scripts to read, plot, and analyze the closure spectra.

In the analysis below, we employ three types of triads:

- EQ14 – short equilateral triads made up of 14.6 m baselines. For example, (0,1,12). A total of 58 triads of this type are analyzed.
- EQ29 – longer equilateral triads of 29.2 m baselines. For example, (0,2,25). A total of 41 triads of this type are analyzed.
- EWs – short East-West triads. For example, (0,1,2). A total of 28 triads of this type are analyzed.

For the equilateral triads, there are two sub-types of redundant triads: those pointing north such as (0,1,12), and those pointing south such as (11,12,1). It is easy to show that the closure phases of these sub-types of north and south facing triads are identical (at least to the level of the redundancy of baselines), if calculated in opposite directions going around the triad (e.g., clockwise for north and counter-clockwise for south), while a calculation of the closure phase going in the same direction around the triads (eg. clockwise for both), leads to a sign change for north vs. south. The analogy for the linear triads would be analyzing, for example, (11,12,13) and (12,13,14).

When including all the redundant triads in the array of a given type as described above, many baselines may be included in more than one triad. Hence, the noise of the closure measurement averaged over redundant triads will not reduce strictly in an uncorrelated manner. However, there may be systematic effects that are reduced by including all the information, and in particular, the baselines on the border of the array that will not get included unless all triads are considered.

5 Results

5.1 Demonstration of calibration-independence of closure spectra

Figure 3 shows examples of visibility phases, and closure phases, versus frequency for one EQ14 triad (121,122,141). Two sets are shown – uncalibrated and calibrated data. The uncalibrated visibility phase spectra show large phase gradients, indicative of large relative delays between antennas. These delays are corrected in the calibrated spectra.

The closure spectra for the uncalibrated and calibrated data are identical to within the numerical accuracy. While this result is as expected, given that sky-calibration is strictly an antenna-based correction, it remains reassuring that: (i) the processing itself does not somehow alter the answer, and (ii) we can employ either calibrated or uncalibrated data in the closure analysis and still obtain information on the true sky signal. In the analysis below, we employ the calibrated and flagged data sets, although, we emphasize that the results are unchanged if using uncalibrated data.

---

[4] http://www.mrao.cam.ac.uk/~bn204/soft/py/heracasa/

5.2 Examples of closure spectra: three fields

In Figure 4, we show images for the three fields analyzed in this study, plus examples of the EWs, EW14, and EW29 closure spectra. The sky calibration and imaging was performed as described in *Carilli and Sims* [2016]; *Nikolic et al.* [2017]. Standard channel-based flagging was performed based on the visibility amplitude spectra.

In brief, the calibration process starts with a delay and mean phase offset calibration using a point source model for the Galactic Center. A CLEAN model is then generated from the delay-calibrated Galactic center data, and the complex bandpass (frequency-dependent, antenna-based gains), is then derived using this CLEAN model. The delay and bandpass corrections are then applied to the visibility data for all three fields for final imaging. We imaged the data using CASA CLEAN, with a Briggs weighting of the visibilities, with a robust parameter of -0.5 [*Briggs and Cornwell*, 1992]. We have employed multi-frequency synthesis across the band 110–190 MHz. The images are not corrected for the power response of the primary beam.

The image of the Galactic Center shows the bright center of the galaxy, and diffuse emission from the Galactic plane extending across the primary beam. The 21 hr field shows clearly the two sources, PMN J2107-2519 and PMN J2101-2802, each within a few arcmin of the expected position (a small fraction of the synthesized beam FWHM of 38'). A few other sources are visible in this field. These are a factor of few weaker than the two bright sources. The 05 hr field shows PMN J0522-3628 clearly. The next brightest four or five sources (yellow to red) in the 21 hr and 05 hr fields have plausible counterparts in the GMRT TGSS [*Intema et al.*, 2017].

We have not performed a rigorous flux scale versus frequency calibration for these data. However, we can do a rough scaling based on the catalog flux density for the source PMN J2101-2801. This source passes closest to the HERA zenith. This source is 2.6° from zenith in the image, or at the 79% power point of the primary beam (assuming an Airy disk for a 14 m antenna at 150MHz). Bootstrapping from J2101-2801, implies an apparent source strength (uncorrected for the primary beam) for PMN J2107-2526 of 16Jy. This source is at the 34% point of the primary beam, and the catalog flux density is 32Jy, so the apparent flux should have been around 11Jy. For J0522-3628 the relevant numbers are an apparent flux density of 13 Jy and an expected apparent flux density (corrected by a factor of 0.22 due to the primary beam) of 16 Jy. For the Galactic Center, the peak surface brightness would then be 52 Jy beam^{-1}, and the total in the field is 350 Jy. We note the rms noise in the 05 hr field is 0.2 Jy beam^{-1}. Overall, the derived flux scaling is good to at best 30%, due to the lack of spectral corrections and detailed knowledge of the primary beam. This scale is not relevant to the closure phase analysis.

As for the closure spectra, it is clear that the frequency structure becomes more pronounced with longer baselines, and more complex sources. For instance, the Galactic Center field is dominated by the main beam emission composed of the bright center of the galaxy, and the smooth extended Galactic plane attenuated by the primary beam. This field shows the smoothest closure spectra. Conversely, the PMN J0522-3628 field has at least six sources of comparable flux density (5 to 10 Jy), and has more pronounced structure in the closure phase spectra. Note these point sources comprise at most 50% of the total flux density in the shorter spacings of the array.

5.3 Redundancy

One of the main goals of this study is to provide a metric for non-redundancy of the array. We have considered both a mean and median analysis when summing closure spectra for redundant triads, and find that the results are the same to within the noise, while the median absolute deviation is comparable to the rms deviation. Given that the median statistic is

generally more robust to outliers, we conservatively adopt the median statistic in the analysis below.

Figure 5 shows the full distribution of closure spectra for all redundant triads of types EQ14, EQ29, and EWs, averaging over 10 records for GC data. We use the GC data to ensure high signal-to-noise over the full spectral range. We also include both up and downward triads for the EQ, calculated in such a way as to sum rather than difference (see §4.3), as well as all the EW short triads. Including all triads ensures that all antennas on the boundaries of the array are included in the summation.

Figure 5 also shows the median for all triads, and the median absolute deviation (approximately the rms scatter at a given frequency), as a function of frequency. While the qualitative behaviour for the redundant triads is similar, it is clear that the systematic difference between triads is much greater than the noise within a given triad. The critical point is that, if all our baselines were exactly redundant, then the curves for redundant triads in Figure 5 would be coincident. Any non-coincidence indicates departures from redundancy.

Figure 6 shows a magnified view of the median absolute deviation of the closure spectra for the three triads in Figure 5. The median absolute deviation is largest for the EWs triad (mean over the frequency range of about 5.8^o), dropping to about $4.5°$ for EQ14, and $3.5°$ for EQ29. There are local peaks by factors of two, but the mean value does not systematically change with frequency. It is interesting that, even though the intrinsic structure in the closure spectra is more complex for the longer EQ29 triads, the departures from redundancy are smaller than for EQ14. This decrease of deviation with longer baselines may indicate an increasing dominance of the brighter sources in the main beam to the longer baseline visibilities, although such differences clearly depend on a specific field brightness distribution, ie. the location and prominence of strong point sources relative to the diffuse continuum. Mutual coupling may also be less for longer baselines.

A point to keep in mind is that any standard antenna-based calibration process, such as redundant calibration or hybrid mapping sky calibration, will not correct for these differences in the closure spectra, i.e., these departures from redundancy will lead to 'closure errors' in the antenna-based calibration process [*Perley*, 1999].

We take $4.5°$ as a representative rms departure from closure redundancy between triads in HERA. We consider how such an error might propagate into visibility errors using antenna-based calibration techniques. We make the simple assumption that the rms phase variations of the visibilities due to e.g., differing primary beams ($\phi_{rms,vis}$), would add in quadrature when calculating closure phase. In this case, the rms phase variations for the closure phases ($\phi_{rms,1,2,3}$), would be: $\phi^2_{rms,1,2,3} = \phi^2_{rms,1,2} + \phi^2_{rms,2,3} + \phi^2_{rms,3,1}$. A value of $\phi_{rms,1,2,3} = 4.5°$ then translates into: $\phi_{rms,vis} = \phi_{rms,triad}/(3^{1/2}) = 2.6°$.

How will non-closing calibration errors of this magnitude affect imaging? The standard relation for image dynamic range due calibration phase errors is given in *Perley* [1999]: $DR \sim N/\phi_{rms,vis}$, where N is the number of antennas and ϕ_{rms} is in radians. For HERA350, the implied image dynamic range limit due to non-closing errors in antenna based calibration schemes is $DR \sim 8000$. For comparison, the highest dynamic range imaging using eg. LOFAR and the VLA has reached a level of order 10^5. However, such studies have been limited to specific fields where the emission is dominated by a strong point source, and in which self-calibration can be performed to the level of hundredths of a degree[*Bernardi et al.*, 2010; *Perley and Meisenheimer*, 2017]. We re-emphasize that our analysis employs commissioning data using prototype electronics. The electronics of the array, including the feeds, will be upgraded in late 2018, after which a reanalysis will be performed.

5.4 Screening ill-behaved antennas

Closure calculations can also be used to find ill-behaved antennas, such as antennas in which the cables for each polarization where inadvertently swapped, in the absence of calibration. Admittedly, such a cross-polarized antenna would also show very low amplitudes, but it remains possible the low amplitudes are due to a low gain somewhere in post-front end signal chain, and hence might normalize-out after calibration. Closure redundancy departures are independent of calibration.

Figure 7 shows the two sets of short linear triads, both EW and oriented 30° from north. The linear east-west triads are: (50, 51, 52) and (51, 52, 53) in black and gray respectively, and the linear triads oriented at 30° are (50, 66, 83) and (51, 67, 84) in orange and red respectively. Triads containing antenna 50 show much higher noise than those that do not. This behaviour was seen in the initial analysis of the data, and it was later found that antenna 50 is cross-polarized. The cross-polarized triads are essentially show noise-like closure phase spanning ±180°.

The main result is that cross-polarized, or otherwise ill-behaved antennas, are very obvious in an analysis of redundant closure spectra, independent of calibration.

5.5 UTC Variation

We next investigate the time variation of the closure spectra over a 10 min observation. The time variation is important in setting the coherent averaging time on which we can perform our cosmological analysis (Thyagarajan et al. 2018). Time variation is due to the sky moving through the primary beam of the transit instrument. We note that the sky moves $\simeq 13°$ at zenith in 1 hour at HERA latitude, and that the FWHM of the HERA beam is 8° at 150 MHz.

Figure 8 shows closure spectra for EQ14, EQ29, and EWs for four consecutive times averaged over 2.5 min each, plus the 10 min averaged closure spectra. There is clear variation of the closure spectra from one 2.5 min time to the next, much larger than the intrinsic scatter.

To investigate this time variation more quantitatively, we have performed an Allan Variance analysis of EQ14 triads on the three different fields (GC, 21 hr, 05 hr). Allan Variance is a standard way of analysing stability of measurement when the instabilities or noise affecting the measurement are non-Gaussian distributed. An introduction to Allan Variance is given by *Thompson et al.* [2017] and an example its application to quantifying stability of astronomical observations is *Schieder and Kramer* [2001]. We computed the Allan deviation of the observed closure phase spectra in order to estimate the time period over which they can be usefully averaged, i.e., before the rotation of the sky introduces a drift larger than the thermal-like noise in the averaged spectrum. The deviation was computed using the overlapping method (see equation 9 and 11, NIST SP 1065 "Handbook of frequency stability analysis") with integration time equal to the stride period.

The results are shown in Figure 9 for the smallest equilateral triad for three different fields. We find a shallow minimum in all cases for delays around 20 sec to 80 sec, beyond which the Allan deviation increases steadily. The correlator dump time of HERA is 10.7s.

5.6 LST Variation

The time variations seen in §5.5 are due to the sky moving through the beam of the transit array. We now investigate variations from one day to the next, but at the same LST, such that the sky position is identical.

Figure 10 shows the closure phase spectra for a single 10.7 s record at the same LST (within 0.4 s), on two consecutive days for the GC observations and the 21 hr source obser-

vations. These spectra are for an EWs triad. The red and black curves are for the two different days. The curves overlap to well within the noise in each case. We then difference the curves from day 1 and day 2. The difference plots are consistent with zero, within the noise. For the GC data we show two examples, separated by 8 min.

Hence, the closure phase spectra appear to be stable at a given LST from one day to the next, at least for the limited amount of data we have analyzed. Stability is critical for coherent averaging of the closure phase spectra from multiple days.

5.7 Closure Amplitudes

For completeness, we calculate closure amplitudes. Closure amplitudes (CA), involve the product of four visibility amplitudes (A_{ij}):

$$CA_{ijkl} = [A_{ij}A_{kl}]/[A_{ik}A_{jl}]$$

As with closure phase, the antenna based calibration terms in this product of visibilities cancel, and one is left with a 'true sky measurement', even for uncalibrated visibilities [see equation 10.44 in *Thompson et al.*, 2017]. The difficulty with analyzing closure amplitudes is that the calculation involves a division, which can lead to divergences around nulls in the visibility functions, for noisy data.

Figure 11 shows the closure amplitudes for two short, redundant quadrangles. These are data from the older HERA-19 array [*Carilli and Nikolic*, 2017; *Carilli and Sims*, 2016].. There is broad similarity between the two quadrangles, but there are large peaks in the distributions that do not replicate well between quadrangles. We have truncated the maximum closure amplitude in the figure. The magnitude of the closure amplitudes go as high as 400.

Figure 11 also shows the visibility amplitude spectra for the baselines in one of these quadrangles. The peaks in the closure amplitude spectra occur when one or more of the visibility spectra approach zero. These figures demonstrate clearly that the closure amplitudes diverge if one of the visibility amplitudes approaches zero.

Two methods may facilitate use of closure amplitudes in the search for the reionization signal. The simplest would be to avoid spectral regions in which one or more visibility spectra approach a null. A related method, in the absence of a wide enough spectral range free of nulls, is to perform an amplitude weighted power spectral analysis, thereby down-weighting spectral regions with low visibility amplitudes.

6 Discussion

We investigate closure phase spectra in the context of the massively redundant, low frequency transit array, HERA. The primary purpose of this work is as supporting material for the potential application of closure phase spectra as a method to detect the H I 21 cm signal from the neutral intergalactic medium during Cosmic Reionization. We consider two important parameters in this regard: temporal stability and array redundancy. More generally, HERA is an excellent laboratory to study the nature of closure and redundancy in interferometry.

We show that, as expected, the closure phase measurements are conserved before and after antenna based calibration, to within the numerical noise. For the fields examined, the closure spectra are relatively smooth with time and frequency (structure on scales of tens of MHz). Spectral complexity increases with complexity of structure in the field and baseline length.

We find that the median absolute deviation of the closure phase measurements between redundant triads in HERA-47 data is about 4.5°, and that this deviation is dominated by triad-to-triad variation, and not signal-to-noise. The deviations from redundancy increase

from the long EQ to the short EQ triads, even though the long baseline triads show more intrinsic structure in the closure spectra. This decrease of deviation with longer baselines may indicate an increasing dominance of the brighter sources in the main beam to the longer baseline visibilities, although this could be field dependent, or due to decreased cross coupling for longer baselines.

The measured deviations provide a rough estimate of the level of redundancy between redundant baselines in HERA. On average, the rms phase deviation between redundant visibilities is about 2.6°. These errors fold directly into calibration errors using standard antenna-based calibration algorithms. We estimate errors of this magnitude would limit the imaging dynamic range of HERA-350 to ~ 8000 using standard antenna-based calibration techniques. We show that closure phase spectra of redundant triads can be used to identify bad antennas, independent of calibration. In our case study, the identified antenna was found to be cross polarized.

Departures from redundancy will clearly affect antenna-based calibration schemes (ie. redundant calibration and sky-based calibration), and affect the power spectral analysis when averaging either redundant visibility spectra or closure spectra. Identifying and removing the worst antennas will help in this process. We emphasize that the analysis presented herein is for a small subset of the HERA antenna, using commissioning electronics for the system. Antennas construction is proceeding to the full 350 complement of antennas, and in late 2018 the entire feed, amplification, data transmission, and back-end system of HERA will be upgraded. Future studies will focus on determining the level of redundancy, using closure techniques, among others, and how departures from redundancy affects the calibration and final cosmological measurement.

We consider the time variation of the closure spectra over the course of an observation. This variation is dominated by the sky moving through beam of the transit telescope. An Allan variance analysis requires an averaging time of less than two minutes, to avoid systematic changes due to sky transit exceeding visibility noise. We also consider changes from day to day at a fixed LST. In this case, the variations are extremely small, much less than the noise in the spectra, and LST binning from day to day will be effective, due to the stable system.

We investigate closure amplitudes. While the behavior for redundant quadrangles are similar, the calculation of closure amplitude involves division, and the values can diverge in regions when one or more of the visibility spectra approaches zero.

In the following papers in the series, we will employ the analysis tools derived herein to the question of H I 21 cm cosmology[*Thyagarajan, Carilli, and Nikolic*, 2018]. In particular, we will attempt to use closure spectra as a robust means to detect the H I 21 cm emission from cosmic reionization, independent of antenna-based calibration and calibration errors, and the ionosphere.

References

Bañados, E., B. P. Venemans, C. Mazzucchelli, E. P. Farina, F. Walter, F. Wang, R. Decarli, D. Stern, X. Fan, F. Davies, J. F. Hennawi, R. Simcoe, M. L. Turner, H. Rix, J. Yang, D. D. Kelson, G. Rudie, and J. M. Winters (2017), An 800 million solar mass black hole in a significantly neutral universe at redshift 7.5, *ArXiv e-prints*.

Baars, J. W. M., R. Genzel, I. I. K. Pauliny-Toth, and A. Witzel (1977), The absolute spectrum of CAS A - an accurate flux density scale and a set of secondary calibrators, A&A, *61*, 99–106.

Barkana, R. (2018), Possible interaction between baryons and dark-matter particles revealed by the first stars, Nature, *555*, 71–74, doi:10.1038/nature25791.

Barkana, R., and A. Loeb (2007), The physics and early history of the intergalactic medium, *Reports on Progress in Physics*, *70*, 627–657, doi:10.1088/0034-4885/70/4/R02.

Beardsley, A. P., B. J. Hazelton, M. F. Morales, W. Arcus, D. Barnes, G. Bernardi, J. D. Bowman, F. H. Briggs, J. D. Bunton, R. J. Cappallo, B. E. Corey, A. Deshpande, L. deSouza, D. Emrich, B. M. Gaensler, R. Goeke, L. J. Greenhill, D. Herne, J. N. Hewitt, M. Johnston-Hollitt, D. L. Kaplan, J. C. Kasper, B. B. Kincaid, R. Koenig, E. Kratzenberg, C. J. Lonsdale, M. J. Lynch, S. R. McWhirter, D. A. Mitchell, E. Morgan, D. Oberoi, S. M. Ord, J. Pathikulangara, T. Prabu, R. A. Remillard, A. E. E. Rogers, A. Roshi, J. E. Salah, R. J. Sault, S. N. Udaya, K. S. Srivani, J. Stevens, R. Subrahmanyan, S. J. Tingay, R. B. Wayth, M. Waterson, R. L. Webster, A. R. Whitney, A. Williams, C. L. Williams, and J. S. B. Wyithe (2013), The EoR sensitivity of the Murchison Widefield Array, MNRAS, *429*, L5–L9, doi:10.1093/mnrasl/sls013.

Bernardi, G., A. G. de Bruyn, G. Harker, M. A. Brentjens, B. Ciardi, V. Jelić, L. V. E. Koopmans, P. Labropoulos, A. Offringa, V. N. Pandey, J. Schaye, R. M. Thomas, S. Yatawatta, and S. Zaroubi (2010), Foregrounds for observations of the cosmological 21 cm line. II. Westerbork observations of the fields around 3C 196 and the North Celestial Pole, A&A, *522*, A67, doi:10.1051/0004-6361/200913420.

Bhatnagar, S., and R. Nityananda (2001), Solving for closure errors due to polarization leakage in radio interferometry of unpolarized sources, A&A, *375*, 344–350, doi:10.1051/0004-6361:20010799.

Bhatnagar, S., R. V. Urvashi, and R. Nityananda (2003), Solving for Polarization Leakage in Radio Interferometers Using Unpolarized Source, in *Astronomical Data Analysis Software and Systems XII*, *Astronomical Society of the Pacific Conference Series*, vol. 295, edited by H. E. Payne, R. I. Jedrzejewski, and R. N. Hook, p. 469.

Bhatnagar, S., T. J. Cornwell, K. Golap, and J. M. Uson (2008), Correcting direction-dependent gains in the deconvolution of radio interferometric images, A&A, *487*, 419–429, doi:10.1051/0004-6361:20079284.

Bowman, J. D., A. E. E. Rogers, R. A. Monsalve, T. J. Mozdzen, and N. Mahesh (2018), An absorption profile centred at 78 megahertz in the sky-averaged spectrum, Nature, *555*, 67–70, doi:10.1038/nature25792.

Briggs, D. S., and T. J. Cornwell (1992), An Alternative Interpretation for the Physical Basis of CLEAN, in *Astronomical Data Analysis Software and Systems I*, *Astronomical Society of the Pacific Conference Series*, vol. 25, edited by D. M. Worrall, C. Biemesderfer, and J. Barnes, p. 170.

Carilli, C. L., and B. Nikolic (2017), HERA memo 35.

Carilli, C. L., and P. Sims (2016), HERA memo 13.

Carilli, C. L., N. Y. Gnedin, and F. Owen (2002), H I 21 Centimeter Absorption beyond the Epoch of Reionization, ApJ, *577*, 22–30, doi:10.1086/342179.

Carilli, C. L., J. C. Pober, and B. Nikolic (2016), HERA memo 15.

Cornwell, T., and E. B. Fomalont (1999), Self-Calibration, in *Synthesis Imaging in Radio Astronomy II*, *Astronomical Society of the Pacific Conference Series*, vol. 180, edited by G. B. Taylor, C. L. Carilli, and R. A. Perley, p. 187.

Datta, A., S. Bhatnagar, and C. L. Carilli (2009), Detection of Signals from Cosmic Reionization Using Radio Interferometric Signal Processing, ApJ, *703*, 1851–1862, doi:10.1088/0004-637X/703/2/1851.

Datta, A., J. D. Bowman, and C. L. Carilli (2010), Bright Source Subtraction Requirements for Redshifted 21 cm Measurements, ApJ, *724*, 526–538, doi:10.1088/0004-637X/724/1/526.

DeBoer, D. R., A. R. Parsons, J. E. Aguirre, P. Alexander, Z. S. Ali, A. P. Beardsley,

G. Bernardi, J. D. Bowman, R. F. Bradley, C. L. Carilli, C. Cheng, E. de Lera Acedo, J. S. Dillon, A. Ewall-Wice, G. Fadana, N. Fagnoni, R. Fritz, S. R. Furlanetto, B. Glendenning, B. Greig, J. Grobbelaar, B. J. Hazelton, J. N. Hewitt, J. Hickish, D. C. Jacobs, A. Julius, M. Kariseb, S. A. Kohn, T. Lekalake, A. Liu, A. Loots, D. MacMahon, L. Malan, C. Malgas, M. Maree, Z. Martinot, N. Mathison, E. Matsetela, A. Mesinger, M. F. Morales, A. R. Neben, N. Patra, S. Pieterse, J. C. Pober, N. Razavi-Ghods, J. Ringuette, J. Robnett, K. Rosie, R. Sell, C. Smith, A. Syce, M. Tegmark, N. Thyagarajan, P. K. G. Williams, and H. Zheng (2017), Hydrogen Epoch of Reionization Array (HERA), PASP, *129*(4), 045,001, doi:10.1088/1538-3873/129/974/045001.

Dillon, J. S., and A. R. Parsons (2016), Redundant Array Configurations for 21 cm Cosmology, ApJ, *826*, 181, doi:10.3847/0004-637X/826/2/181.

Ewall-Wice, A., R. Bradley, D. Deboer, J. Hewitt, A. Parsons, J. Aguirre, Z. S. Ali, J. Bowman, C. Cheng, A. R. Neben, N. Patra, N. Thyagarajan, M. Venter, E. de Lera Acedo, J. S. Dillon, R. Dickenson, P. Doolittle, D. Egan, M. Hedrick, P. Klima, S. Kohn, P. Schaffner, J. Shelton, B. Saliwanchik, H. A. Taylor, R. Taylor, M. Tegmark, and B. Wirt (2016), The Hydrogen Epoch of Reionization Array Dish. II. Characterization of Spectral Structure with Electromagnetic Simulations and Its Science Implications., ApJ, *831*, 196, doi: 10.3847/0004-637X/831/2/196.

Fan, X., C. L. Carilli, and B. Keating (2006), Observational Constraints on Cosmic Reionization, ARA&A, *44*, 415–462, doi:10.1146/annurev.astro.44.051905.092514.

Fomalont, E. B., and R. A. Perley (1999), Calibration and Editing, in *Synthesis Imaging in Radio Astronomy II*, *Astronomical Society of the Pacific Conference Series*, vol. 180, edited by G. B. Taylor, C. L. Carilli, and R. A. Perley, p. 79.

Gehlot, B. K., L. V. E. Koopmans, A. G. de Bruyn, S. Zaroubi, M. A. Brentjens, K. M. B. Asad, M. Hatef, V. Jelic, M. Mevius, A. R. Offringa, V. N. Pandey, and S. Yatawatta (2017), Wide-field LOFAR-LBA power-spectra analyses: Impact of calibration, polarization leakage and ionosphere, *ArXiv e-prints*.

Greig, B., and A. Mesinger (2017), Simultaneously constraining the astrophysics of reionization and the epoch of heating with 21CMMC, MNRAS, *472*, 2651–2669, doi:10.1093/mnras/stx2118.

Hashimoto, I., Y. Rasera, and A. Taruya (2017), Precision cosmology with redshift-space bispectrum: A perturbation theory based model at one-loop order, Phys. Rev. D, *96*(4), 043526, doi:10.1103/PhysRevD.96.043526.

Hazelton, B., D. Jacobs, J. Pober, and A. Beardsley (2017), pyuvdata: an interface for astronomical interferometeric datasets in python, *Journal of Open Source Software*, *2*(10), 140, doi:10.21105/joss.00140.

Hurley-Walker, N., J. R. Callingham, P. J. Hancock, T. M. O. Franzen, L. Hindson, A. D. Kapińska, J. Morgan, A. R. Offringa, R. B. Wayth, C. Wu, Q. Zheng, T. Murphy, M. E. Bell, K. S. Dwarakanath, B. For, B. M. Gaensler, M. Johnston-Hollitt, E. Lenc, P. Procopio, L. Staveley-Smith, R. Ekers, J. D. Bowman, F. Briggs, R. J. Cappallo, A. A. Deshpande, L. Greenhill, B. J. Hazelton, D. L. Kaplan, C. J. Lonsdale, S. R. McWhirter, D. A. Mitchell, M. F. Morales, E. Morgan, D. Oberoi, S. M. Ord, T. Prabu, N. U. Shankar, K. S. Srivani, R. Subrahmanyan, S. J. Tingay, R. L. Webster, A. Williams, and C. L. Williams (2017), GaLactic and Extragalactic All-sky Murchison Widefield Array (GLEAM) survey - I. A low-frequency extragalactic catalogue, MNRAS, *464*, 1146–1167, doi: 10.1093/mnras/stw2337.

Iliev, I. T., P. R. Shapiro, A. Ferrara, and H. Martel (2002), On the Direct Detectability of the Cosmic Dark Ages: 21 Centimeter Emission from Minihalos, ApJ, *572*, L123–L126, doi:10.1086/341869.

Intema, H. T., P. Jagannathan, K. P. Mooley, and D. A. Frail (2017), The GMRT 150 MHz all-sky radio survey. First alternative data release TGSS ADR1, A&A, *598*, A78, doi:10. 1051/0004-6361/201628536.

Jennison, R. C. (1958), A phase sensitive interferometer technique for the measurement of the Fourier transforms of spatial brightness distributions of small angular extent, MNRAS,

118, 276, doi:10.1093/mnras/118.3.276.

Johnson, M. D., K. L. Bouman, L. Blackburn, A. A. Chael, J. Rosen, H. Shiokawa, F. Roelofs, K. Akiyama, V. L. Fish, and S. S. Doeleman (2017), Dynamical Imaging with Interferometry, ApJ, *850*, 172, doi:10.3847/1538-4357/aa97dd.

Kassim, N. E., T. J. W. Lazio, W. C. Erickson, R. A. Perley, W. D. Cotton, E. W. Greisen, A. S. Cohen, B. Hicks, H. R. Schmitt, and D. Katz (2007), The 74 MHz System on the Very Large Array, ApJS, *172*, 686–719, doi:10.1086/519022.

Kulkarni, S. R. (1989), Self-noise in interferometers - Radio and infrared, AJ, *98*, 1112–1130, doi:10.1086/115202.

Liu, A., A. R. Parsons, and C. M. Trott (2014), Epoch of reionization window. I. Mathematical formalism, Phys. Rev. D, *90*(2), 023018, doi:10.1103/PhysRevD.90.023018.

Madau, P., A. Meiksin, and M. J. Rees (1997), 21 Centimeter Tomography of the Intergalactic Medium at High Redshift, ApJ, *475*, 429–444, doi:10.1086/303549.

McMullin, J. P., B. Waters, D. Schiebel, W. Young, and K. Golap (2007), CASA Architecture and Applications, in *Astronomical Data Analysis Software and Systems XVI*, *Astronomical Society of the Pacific Conference Series*, vol. 376, edited by R. A. Shaw, F. Hill, and D. J. Bell, p. 127.

Mertens, F. G., A. Ghosh, and L. V. E. Koopmans (2017), Statistical 21-cm Signal Separation via Gaussian Process Regression Analysis, *ArXiv e-prints*.

Mevius, M., S. van der Tol, V. N. Pandey, H. K. Vedantham, M. A. Brentjens, A. G. de Bruyn, F. B. Abdalla, K. M. B. Asad, J. D. Bregman, W. N. Brouw, S. Bus, E. Chapman, B. Ciardi, E. R. Fernandez, A. Ghosh, G. Harker, I. T. Iliev, V. Jelić, S. Kazemi, L. V. E. Koopmans, J. E. Noordam, A. R. Offringa, A. H. Patil, R. J. van Weeren, S. Wijnholds, S. Yatawatta, and S. Zaroubi (2016), Probing ionospheric structures using the LOFAR radio telescope, *Radio Science*, *51*, 927–941, doi:10.1002/2016RS006028.

Monnier, J. D. (2007), Phases in interferometry, New A Rev., *51*, 604–616, doi:10.1016/j.newar.2007.06.006.

Monsalve, R. A., A. E. E. Rogers, J. D. Bowman, and T. J. Mozdzen (2017), Results from EDGES High-band. I. Constraints on Phenomenological Models for the Global 21 cm Signal, ApJ, *847*, 64, doi:10.3847/1538-4357/aa88d1.

Morales, M. F., and J. S. B. Wyithe (2010), Reionization and Cosmology with 21-cm Fluctuations, ARA&A, *48*, 127–171, doi:10.1146/annurev-astro-081309-130936.

Morales, M. F., B. Hazelton, I. Sullivan, and A. Beardsley (2012), Four Fundamental Foreground Power Spectrum Shapes for 21 cm Cosmology Observations, ApJ, *752*, 137, doi:10.1088/0004-637X/752/2/137.

Neben, A. R., R. F. Bradley, J. N. Hewitt, D. R. DeBoer, A. R. Parsons, J. E. Aguirre, Z. S. Ali, C. Cheng, A. Ewall-Wice, N. Patra, N. Thyagarajan, J. Bowman, R. Dickenson, J. S. Dillon, P. Doolittle, D. Egan, M. Hedrick, D. C. Jacobs, S. A. Kohn, P. J. Klima, K. Moodley, B. R. B. Saliwanchik, P. Schaffner, J. Shelton, H. A. Taylor, R. Taylor, M. Tegmark, B. Wirt, and H. Zheng (2016), The Hydrogen Epoch of Reionization Array Dish. I. Beam Pattern Measurements and Science Implications, ApJ, *826*, 199, doi:10.3847/0004-637X/826/2/199.

Nikolic, B., C. Carilli, and HERA Collaboration (2017), Self-calibration of highly-redundant low-frequency arrays - initial results with HERA, *ArXiv e-prints*.

Pacholczyk, A. G. (1970), *Radio astrophysics. Nonthermal processes in galactic and extragalactic sources*.

Parsons, A. R., J. C. Pober, J. E. Aguirre, C. L. Carilli, D. C. Jacobs, and D. F. Moore (2012), A Per-baseline, Delay-spectrum Technique for Accessing the 21 cm Cosmic Reionization Signature, ApJ, *756*, 165, doi:10.1088/0004-637X/756/2/165.

Patil, A. H., S. Yatawatta, L. V. E. Koopmans, A. G. de Bruyn, M. A. Brentjens, S. Zaroubi, K. M. B. Asad, M. Hatef, V. Jelić, M. Mevius, A. R. Offringa, V. N. Pandey, H. Vedantham, F. B. Abdalla, W. N. Brouw, E. Chapman, B. Ciardi, B. K. Gehlot, A. Ghosh, G. Harker, I. T. Iliev, K. Kakiichi, S. Majumdar, G. Mellema, M. B. Silva, J. Schaye, D. Vrbanec, and S. J. Wijnholds (2017), Upper Limits on the 21 cm Epoch of Reionization

Power Spectrum from One Night with LOFAR, ApJ, *838*, 65, doi:10.3847/1538-4357/aa63e7.

Patra, N., A. R. Parsons, D. R. DeBoer, N. Thyagarajan, A. Ewall-Wice, G. Hsyu, T. Kuk Leung, C. K. Day, J. E. Aguirre, P. Alexander, Z. S. Ali, A. P. Beardsley, J. D. Bowman, R. F. Bradley, C. L. Carilli, C. Cheng, E. de Lera Acedo, J. S. Dillon, G. Fadana, N. Fagnoni, R. Fritz, S. R. Furlanetto, B. Glendenning, B. Greig, J. Grobbelaar, B. J. Hazelton, J. N. Hewitt, D. C. Jacobs, A. Julius, M. Kariseb, S. A. Kohn, A. Lebedeva, T. Lekalake, A. Liu, A. Loots, D. MacMahon, L. Malan, C. Malgas, M. Maree, Z. Martinot, N. Mathison, E. Matsetela, A. Mesinger, M. F. Morales, A. R. Neben, S. Pieterse, J. C. Pober, N. Razavi-Ghods, J. Ringuette, J. Robnett, K. Rosie, R. Sell, C. Smith, A. Syce, M. Tegmark, P. K. G. Williams, and H. Zheng (2017), The Hydrogen Epoch of Reionization Array Dish III: Measuring Chromaticity of Prototype Element with Reflectometry, *ArXiv e-prints*.

Pearson, T. J., and A. C. S. Readhead (1984), Image Formation by Self-Calibration in Radio Astronomy, ARA&A, *22*, 97–130, doi:10.1146/annurev.aa.22.090184.000525.

Perley, R. A. (1999), High Dynamic Range Imaging, in *Synthesis Imaging in Radio Astronomy II*, *Astronomical Society of the Pacific Conference Series*, vol. 180, edited by G. B. Taylor, C. L. Carilli, and R. A. Perley, p. 275.

Perley, R. A., and K. Meisenheimer (2017), High-fidelity VLA imaging of the radio structure of 3C 273, A&A, *601*, A35, doi:10.1051/0004-6361/201629704.

Pober, J. C., A. R. Parsons, J. E. Aguirre, Z. Ali, R. F. Bradley, C. L. Carilli, D. DeBoer, M. Dexter, N. E. Gugliucci, D. C. Jacobs, P. J. Klima, D. MacMahon, J. Manley, D. F. Moore, I. I. Stefan, and W. P. Walbrugh (2013), Opening the 21 cm Epoch of Reionization Window: Measurements of Foreground Isolation with PAPER, ApJ, *768*, L36, doi:10.1088/2041-8205/768/2/L36.

Pober, J. C., B. J. Hazelton, A. P. Beardsley, N. A. Barry, Z. E. Martinot, I. S. Sullivan, M. F. Morales, M. E. Bell, G. Bernardi, N. D. R. Bhat, J. D. Bowman, F. Briggs, R. J. Cappallo, P. Carroll, B. E. Corey, A. de Oliveira-Costa, A. A. Deshpande, J. S. Dillon, D. Emrich, A. M. Ewall-Wice, L. Feng, R. Goeke, L. J. Greenhill, J. N. Hewitt, L. Hindson, N. Hurley-Walker, D. C. Jacobs, M. Johnston-Hollitt, D. L. Kaplan, J. C. Kasper, H.-S. Kim, P. Kittiwisit, E. Kratzenberg, N. Kudryavtseva, E. Lenc, J. Line, A. Loeb, C. J. Lonsdale, M. J. Lynch, B. McKinley, S. R. McWhirter, D. A. Mitchell, E. Morgan, A. R. Neben, D. Oberoi, A. R. Offringa, S. M. Ord, S. Paul, B. Pindor, T. Prabu, P. Procopio, J. Riding, A. E. E. Rogers, A. Roshi, S. K. Sethi, N. Udaya Shankar, K. S. Srivani, R. Subrahmanyan, M. Tegmark, N. Thyagarajan, S. J. Tingay, C. M. Trott, M. Waterson, R. B. Wayth, R. L. Webster, A. R. Whitney, A. Williams, C. L. Williams, and J. S. B. Wyithe (2016), The Importance of Wide-field Foreground Removal for 21 cm Cosmology: A Demonstration With Early MWA Epoch of Reionization Observations, *ArXiv e-prints*.

Readhead, A. C. S., and P. N. Wilkinson (1978), The mapping of compact radio sources from VLBI data, ApJ, *223*, 25–36, doi:10.1086/156232.

Robertson, B. E., R. S. Ellis, S. R. Furlanetto, and J. S. Dunlop (2015), Cosmic Reionization and Early Star-forming Galaxies: A Joint Analysis of New Constraints from Planck and the Hubble Space Telescope, ApJ, *802*, L19, doi:10.1088/2041-8205/802/2/L19.

Roelofs, F., M. D. Johnson, H. Shiokawa, S. S. Doeleman, and H. Falcke (2017), Quantifying Intrinsic Variability of Sagittarius A* Using Closure Phase Measurements of the Event Horizon Telescope, ApJ, *847*, 55, doi:10.3847/1538-4357/aa8455.

Rogers, A. E. E., H. F. Hinteregger, A. R. Whitney, C. C. Counselman, I. I. Shapiro, J. J. Wittels, W. K. Klemperer, W. W. Warnock, T. A. Clark, L. K. Hutton, G. E. Marandino, B. O. Ronnang, O. E. H. Rydbeck, and A. E. Niell (1974), The structure of radio sources 3C 273B and 3C 84 deduced from the 'closure' phases and visibility amplitudes observed with three-element interferometers, ApJ, *193*, 293–301, doi:10.1086/153162.

Rupen, M. P. (1999), Spectral Line Observing II: Calibration and Analysis, in *Synthesis Imaging in Radio Astronomy II*, *Astronomical Society of the Pacific Conference Series*, vol. 180, edited by G. B. Taylor, C. L. Carilli, and R. A. Perley, p. 229.

Schieder, R., and C. Kramer (2001), Optimization of heterodyne observations using Allan variance measurements, A&A, *373*, 746–756, doi:10.1051/0004-6361:20010611.

Scott, D., and M. J. Rees (1990), The 21-cm line at high redshift: a diagnostic for the origin of large scale structure, MNRAS, *247*, 510.

Sims, P. H., L. Lentati, P. Alexander, and C. L. Carilli (2016), Contamination of the Epoch of Reionization power spectrum in the presence of foregrounds, MNRAS, *462*, 3069–3093, doi:10.1093/mnras/stw1768.

Smirnov, O. M. (2011), Revisiting the radio interferometer measurement equation. I. A full-sky Jones formalism, A&A, *527*, A106, doi:10.1051/0004-6361/201016082.

Smirnov, O. M., and C. Tasse (2015), Radio interferometric gain calibration as a complex optimization problem, MNRAS, *449*, 2668–2684, doi:10.1093/mnras/stv418.

Song, Y.-S., A. Taruya, and A. Oka (2015), Cosmology with anisotropic galaxy clustering from the combination of power spectrum and bispectrum, J. Cosmology Astropart. Phys., *8*, 007, doi:10.1088/1475-7516/2015/08/007.

Sunyaev, R. A., and Y. B. Zeldovich (1972), Formation of Clusters of Galaxies; Protocluster Fragmentation and Intergalactic Gas Heating, A&A, *20*, 189.

Thiebaut, E., and J.-F. Giovannelli (2010), Image reconstruction in optical interferometry, *IEEE Signal Processing Magazine*, *27*, 97–109, doi:10.1109/MSP.2009.934870.

Thompson, A. R. (1999), Fundamentals of Radio Interferometry, in *Synthesis Imaging in Radio Astronomy II*, *Astronomical Society of the Pacific Conference Series*, vol. 180, edited by G. B. Taylor, C. L. Carilli, and R. A. Perley, p. 11.

Thompson, A. R., J. M. Moran, and G. W. Swenson, Jr. (2017), *Interferometry and Synthesis in Radio Astronomy, 3rd Edition*, doi:10.1007/978-3-319-44431-4.

Thayagarajan, N., C.L. Carilli, and B. Nikolic (2018), Detecting Cosmic Reionization using Bi-Spectrum Phase, *Physical Review Letters*, in press.

Thyagarajan, N., N. Udaya Shankar, R. Subrahmanyan, W. Arcus, G. Bernardi, J. D. Bowman, F. Briggs, J. D. Bunton, R. J. Cappallo, B. E. Corey, L. deSouza, D. Emrich, B. M. Gaensler, R. F. Goeke, L. J. Greenhill, B. J. Hazelton, D. Herne, J. N. Hewitt, M. Johnston-Hollitt, D. L. Kaplan, J. C. Kasper, B. B. Kincaid, R. Koenig, E. Kratzenberg, C. J. Lonsdale, M. J. Lynch, S. R. McWhirter, D. A. Mitchell, M. F. Morales, E. H. Morgan, D. Oberoi, S. M. Ord, J. Pathikulangara, R. A. Remillard, A. E. E. Rogers, D. Anish Roshi, J. E. Salah, R. J. Sault, K. S. Srivani, J. B. Stevens, P. Thiagaraj, S. J. Tingay, R. B. Wayth, M. Waterson, R. L. Webster, A. R. Whitney, A. J. Williams, C. L. Williams, and J. S. B. Wyithe (2013), A Study of Fundamental Limitations to Statistical Detection of Redshifted H I from the Epoch of Reionization, ApJ, *776*, 6, doi:10.1088/0004-637X/776/1/6.

Thyagarajan, N., D. C. Jacobs, J. D. Bowman, N. Barry, A. P. Beardsley, G. Bernardi, F. Briggs, R. J. Cappallo, P. Carroll, B. E. Corey, A. de Oliveira-Costa, J. S. Dillon, D. Emrich, A. Ewall-Wice, L. Feng, R. Goeke, L. J. Greenhill, B. J. Hazelton, J. N. Hewitt, N. Hurley-Walker, M. Johnston-Hollitt, D. L. Kaplan, J. C. Kasper, H.-S. Kim, P. Kittiwisit, E. Kratzenberg, E. Lenc, J. Line, A. Loeb, C. J. Lonsdale, M. J. Lynch, B. McKinley, S. R. McWhirter, D. A. Mitchell, M. F. Morales, E. Morgan, A. R. Neben, D. Oberoi, A. R. Offringa, S. M. Ord, S. Paul, B. Pindor, J. C. Pober, T. Prabu, P. Procopio, J. Riding, A. E. E. Rogers, A. Roshi, N. Udaya Shankar, S. K. Sethi, K. S. Srivani, R. Subrahmanyan, I. S. Sullivan, M. Tegmark, S. J. Tingay, C. M. Trott, M. Waterson, R. B. Wayth, R. L. Webster, A. R. Whitney, A. Williams, C. L. Williams, C. Wu, and J. S. B. Wyithe (2015a), Foregrounds in Wide-field Redshifted 21 cm Power Spectra, ApJ, *804*, 14, doi:10.1088/0004-637X/804/1/14.

Thyagarajan, N., D. C. Jacobs, J. D. Bowman, N. Barry, A. P. Beardsley, G. Bernardi, F. Briggs, R. J. Cappallo, P. Carroll, A. A. Deshpande, A. de Oliveira-Costa, J. S. Dillon, A. Ewall-Wice, L. Feng, L. J. Greenhill, B. J. Hazelton, L. Hernquist, J. N. Hewitt, N. Hurley-Walker, M. Johnston-Hollitt, D. L. Kaplan, H.-S. Kim, P. Kittiwisit, E. Lenc, J. Line, A. Loeb, C. J. Lonsdale, B. McKinley, S. R. McWhirter, D. A. Mitchell, M. F. Morales, E. Morgan, A. R. Neben, D. Oberoi, A. R. Offringa, S. M. Ord, S. Paul, B. Pin-

dor, J. C. Pober, T. Prabu, P. Procopio, J. Riding, N. Udaya Shankar, S. K. Sethi, K. S. Srivani, R. Subrahmanyan, I. S. Sullivan, M. Tegmark, S. J. Tingay, C. M. Trott, R. B. Wayth, R. L. Webster, A. Williams, C. L. Williams, and J. S. B. Wyithe (2015b), Confirmation of Wide-field Signatures in Redshifted 21 cm Power Spectra, ApJ, *807*, L28, doi:10.1088/2041-8205/807/2/L28.

Thyagarajan, N., A. R. Parsons, D. R. DeBoer, J. D. Bowman, A. M. Ewall-Wice, A. R. Neben, and N. Patra (2016), Effects of Antenna Beam Chromaticity on Redshifted 21 cm Power Spectrum and Implications for Hydrogen Epoch of Reionization Array, ApJ, *825*, 9, doi:10.3847/0004-637X/825/1/9.

Tozzi, P., P. Madau, A. Meiksin, and M. J. Rees (2000), Radio Signatures of H I at High Redshift: Mapping the End of the "Dark Ages", ApJ, *528*, 597–606, doi:10.1086/308196.

Trott, C. M., R. B. Wayth, and S. J. Tingay (2012), The Impact of Point-source Subtraction Residuals on 21 cm Epoch of Reionization Estimation, ApJ, *757*, 101, doi:10.1088/0004-637X/757/1/101.

Trott, C. M., B. Pindor, P. Procopio, R. B. Wayth, D. A. Mitchell, B. McKinley, S. J. Tingay, N. Barry, A. P. Beardsley, G. Bernardi, J. D. Bowman, F. Briggs, R. J. Cappallo, P. Carroll, A. de Oliveira-Costa, J. S. Dillon, A. Ewall-Wice, L. Feng, L. J. Greenhill, B. J. Hazelton, J. N. Hewitt, N. Hurley-Walker, M. Johnston-Hollitt, D. C. Jacobs, D. L. Kaplan, H. S. Kim, E. Lenc, J. Line, A. Loeb, C. J. Lonsdale, M. F. Morales, E. Morgan, A. R. Neben, N. Thyagarajan, D. Oberoi, A. R. Offringa, S. M. Ord, S. Paul, J. C. Pober, T. Prabu, J. Riding, N. Udaya Shankar, S. K. Sethi, K. S. Srivani, R. Subrahmanyan, I. S. Sullivan, M. Tegmark, R. L. Webster, A. Williams, C. L. Williams, C. Wu, and J. S. B. Wyithe (2016), CHIPS: The Cosmological H I Power Spectrum Estimator, ApJ, *818*, 139, doi:10.3847/0004-637X/818/2/139.

Vedantham, H., N. Udaya Shankar, and R. Subrahmanyan (2012), Imaging the Epoch of Reionization: Limitations from Foreground Confusion and Imaging Algorithms, ApJ, *745*, 176, doi:10.1088/0004-637X/745/2/176.
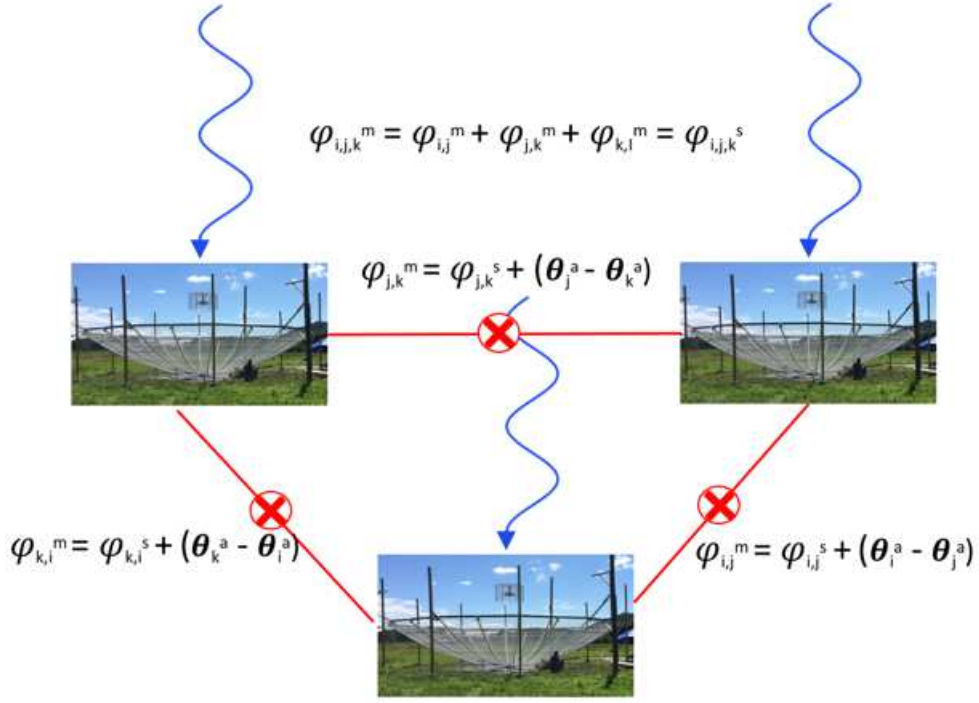
Figure 1. Schematic of the closure phase calculation for a three-element interferometer with elements i, j, k. ϕ^m is the frequency-dependent measured phase of a visibility (cross-correlation of voltages), between two antennas. ϕ^s is the true sky value of the phase (i.e., uncorrupted by the response of the system). θ^a is the electronic phase term introduced by each antenna, including the contribution to the electronic path-length by the atmosphere above each antenna. Assuming that the electronic response of the system can be factorized into antenna-based terms, θ^a, then, in the sum of the measured interferometric phases around any triad of antennas, these antenna-based phase terms cancel, leaving a 'true' sky measurement, modulo a thermal noise term that is not shown explicitly.

Figure 2. An aerial view of the first 19 antennas showing the grid pattern (Top) and positions and antenna numbers for HERA-47 in October 2017 (Bottom). The PAPER antennas and the MEERKAT array are visible in the background in the upper picture. The lower figure is one of the standard diagnostic plots produced by the HERA on-line system. Greendots indicate whether both polarizations were installed, and the antenna numbers are listed to the upper right of each antenna. The other number/letter combinations are internal diagnostic identifiers for electronic elements in the system.

(a)

(b)

(c)

(d)

Figure 3. Left: Visibility phase spectra for three antennas in a short equilateral triad (Top: uncalibrated, Bottom: delay and bandpass calibrated). Right: Resulting closure phase spectrum. The measured closure phases are independent of antenna-based calibration of visibilities. These data correspond to the Galactic Center region.

(a) Galactic Center field image

(b) Galactic Center field closure phase

(c) 21 hr field image

(d) 21 hr field closure phase

(e) 05 hr field image

(f) 05 hr field closure phase
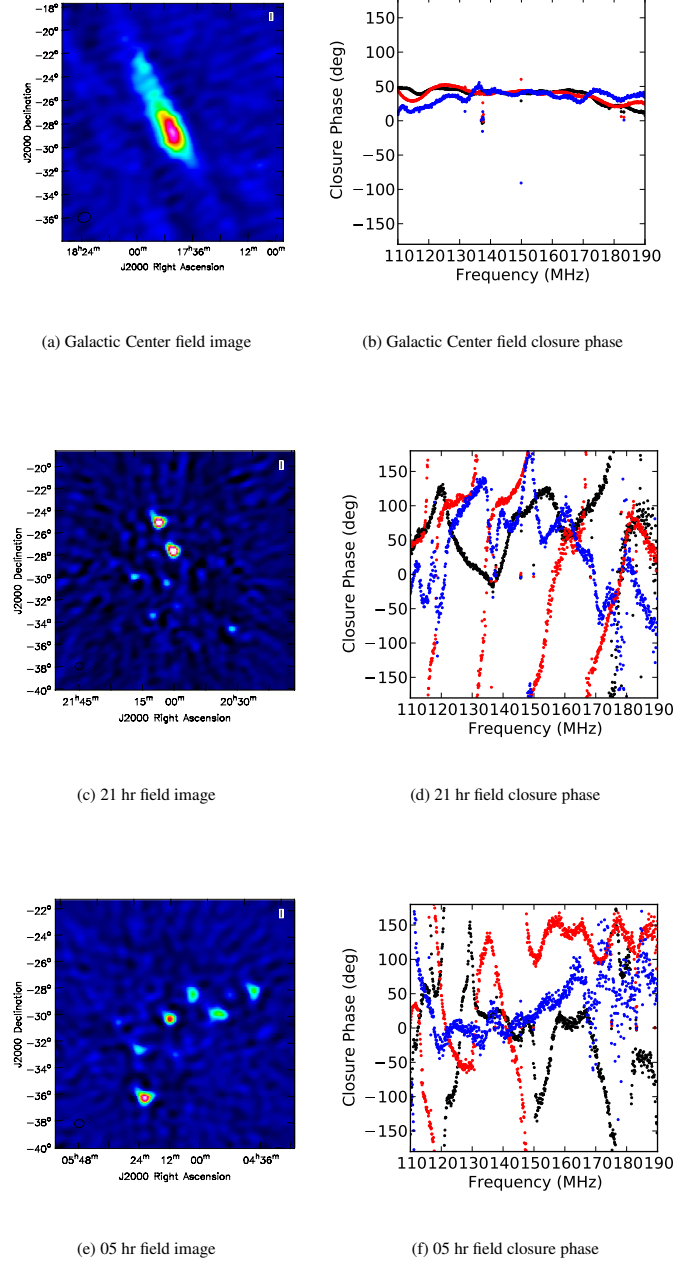
Figure 4. Top left: The HERA-47 image of the Galactic Center region at 150 MHz, with a synthesized beam of FWHM = 38′. Top right: Closure phase spectra on three representative triads averaged over 1 min: black = short east-west (EWs), e.g., (0,1,2); red = 14m equilateral (EQ14), e.g., (0,1,12), and blue = 29m equilateral (EQ29), e.g., (0,2,25). Middle: Same, but for the 21 hr source field. Bottom: Same, but for the 05 hr field. Note that the next brightest four or five sources (yellow to red) in the 21 hr and 05 hr fields have plausible counterparts in the GMRT TGSS [*Intema et al.*, 2017].
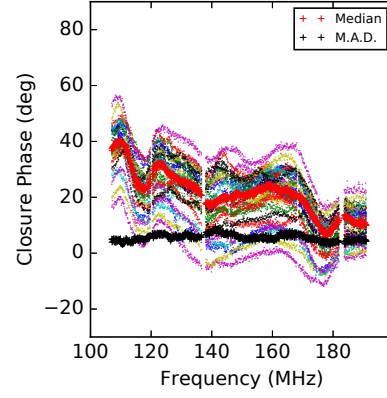
(a) EWs triads
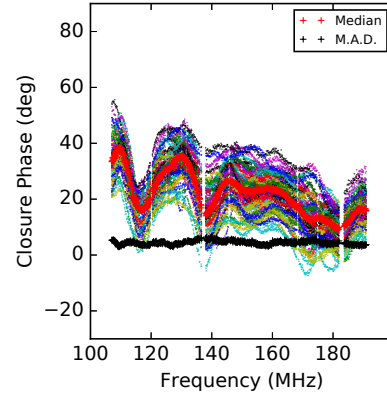
(b) EQ14 triads
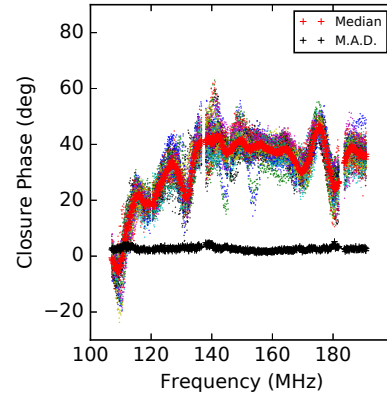
(c) EQ29 triads

Figure 5. Top: Median (bold red) and median absolute deviation (black) for closure phase spectra on the GC field for EWs triads, calculated across all redundant triads of this type, and for spectra averaged over 1 min. The data for each triad is also shown independently in lighter colors, to demonstrate the scatter between redundant triads. Middle: Same, but for EQ14 triads. Bottom: Same, but for EQ29 triads.
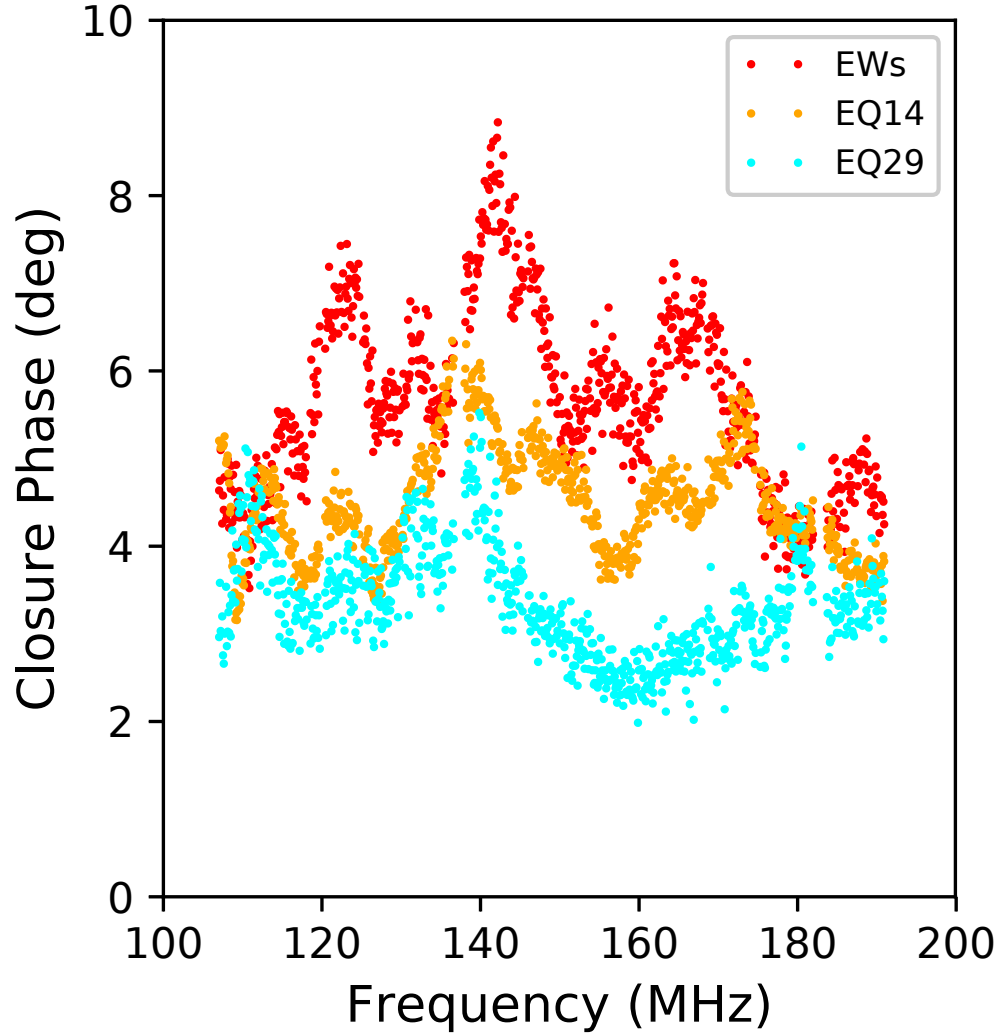
Figure 6. The median absolute deviation between redundant triads versus frequency from figure 7. The three triads are show in different colors. The deviations for the EQ29 triads are smaller than the EQ14 triads. Larger deviations from redundancy for longer baseline triads may be due to the longer baselines being more sensitive to bright sources in the main beam, where antenna to antenna beam differences may be less than for the more distant sidelobes of the antenna beam. The shorter triads have a larger contribution from diffuse emission, which fills both the main beam and the far sidelobes, although this phenomenon is likely field-dependent.
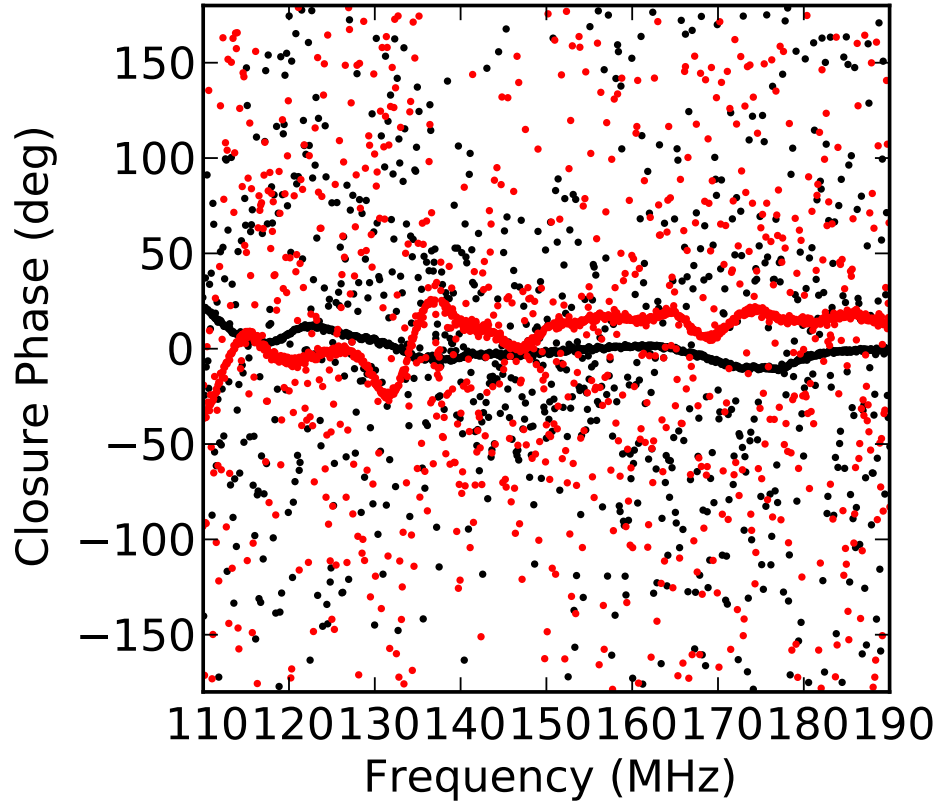
Figure 7. The black curve shows the EWs linear triad closure spectrum for the triad (51,52,53), while the black points show a similar curve for EWs triad (50,51,52). The red curve is for a short linear triad (51,67,84), but oriented 30° from north, and the red points are for a linear triad of the same orientation but formed from antennas (50,66,83). These are for Galactic Center data with 60 s averaging. Antenna 50 was found to be cross-polarized and hence triads that include this antenna show noise-like closure phase spanning ±180°.
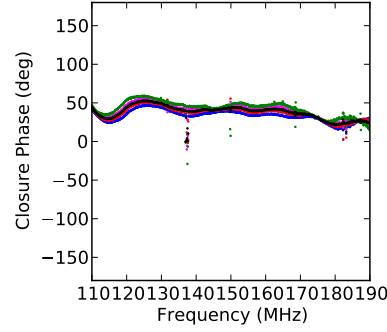
(a) Galactic Center field
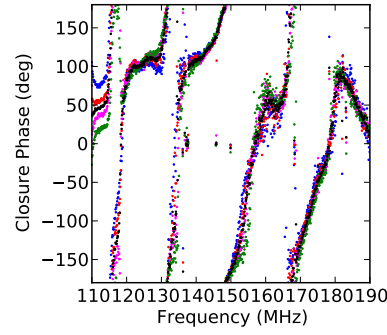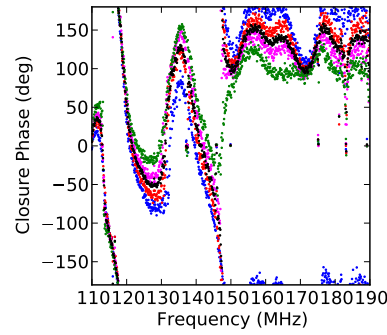
(b) 21 hr field

(c) 05 hr field

Figure 8. Top: Closure spectra for an EQ14 triad on Galactic Center data. The red-blue-magenta-green curves are consecutive 2.5 min averaged spectra. The black is the spectrum averaged over 10 min. Middle: Same, but for the 21 hr field. Bottom: Same, but for the 05 hr field. The variation across 2.5 min intervals is found to exceed intrinsic scatter in each of the intervals.
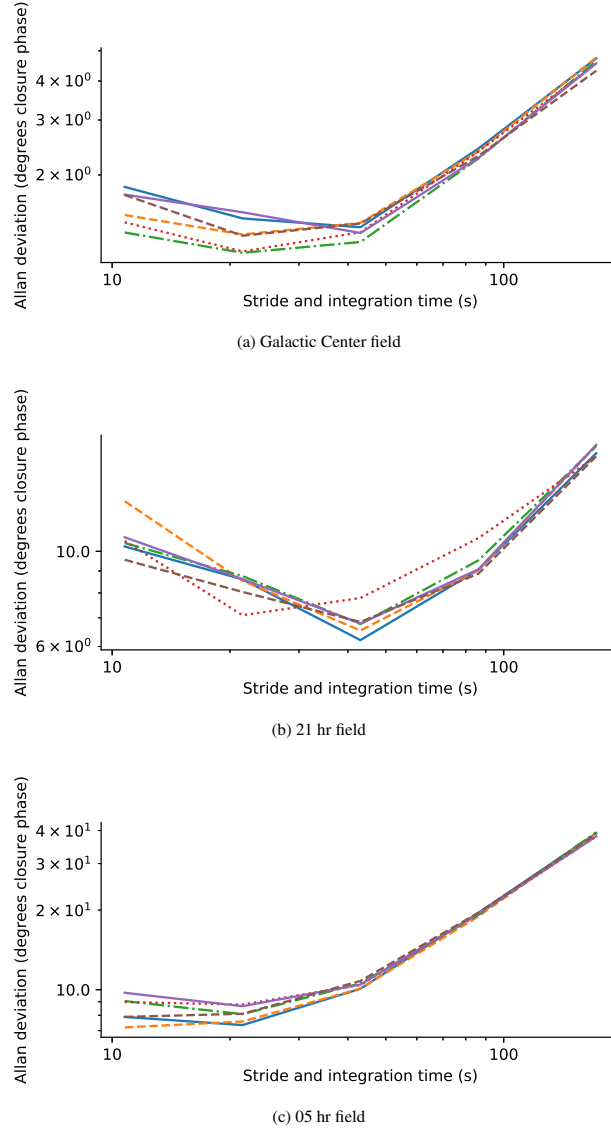
(a) Galactic Center field

(b) 21 hr field

(c) 05 hr field

Figure 9. Allan standard deviations of the closure phase on the East-West triad for: (top panel) the Galactic Centre field; (middle panel) the 21h field and (lower panel) the 5h field. Each panel shows the Allan standard deviation for 6 neighbouring frequency channels (shown by the 6 lines in each panel) at around 140 MHz. Beyond a timescale of 20–80 s, the difference caused by the drifting of sky becomes larger than the noise level in closure phases, which are dominant on shorter timescales.
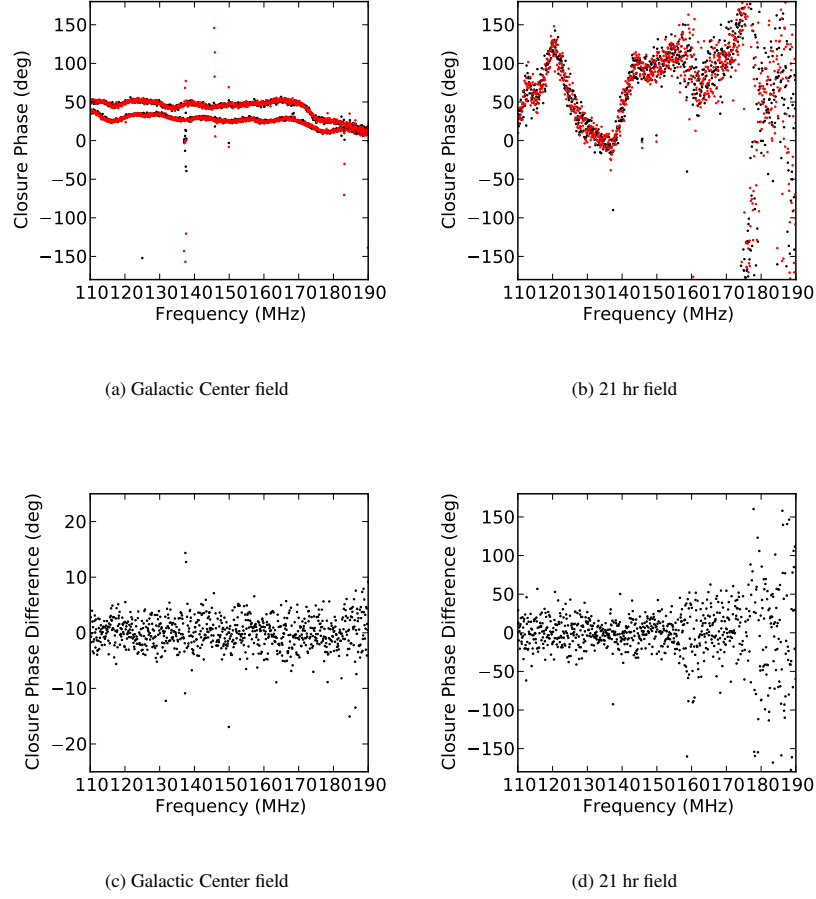
(a) Galactic Center field

(b) 21 hr field

(c) Galactic Center field

(d) 21 hr field

Figure 10. Top left: Closure spectra for an EWs triad for GC data for a 10.7 s record, from the same LST on two consecutive days. Two examples are shown, separated by 8 min. The red and black curves are for day 1 and 2. Top right: same but for the 21 hr field. Bottom left: Difference between closure phase spectra from two 10.7 s records on consecutive days for the GC data and an EWs triad. Bottom right: Same, but for the 21 hr field. The difference between closure phases at same LST on consecutive days is consistent with expected closure phase noise rms.
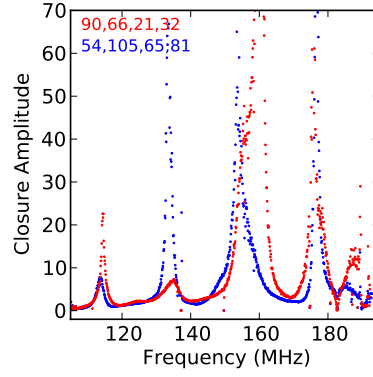
(a) Closure amplitudes
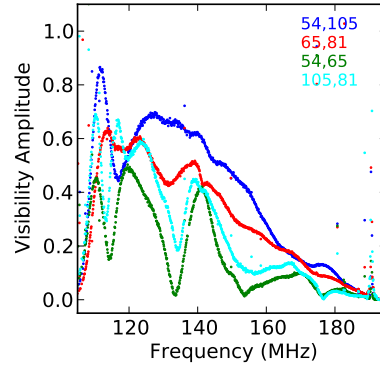
(b) Visibility amplitudes

Figure 11. Top: Closure Amplitude spectra for two short, redundant quadrangles for GC data from the HERA19 configuration [see *Carilli and Sims*, 2016]. We have truncated the maximum closure amplitude in the figure. The closure amplitude magnitudes go up to 400. Bottom: The calibrated visibility amplitude spectra for one set of four antennas used in the closure amplitude spectrum. The frequency range is 100MHz to 200MHz. The high-valued closure amplitudes in the spectra are caused by and coincide with low-valued visibility amplitudes.